41st AIAA Fluid Dynamics Conference and Exhibit
27 - 30 June 2011, Honolulu, Hawaii

AIAA 2011-3078

Numerical Study of Freestream Hot-Spot Perturbation on Boundary-Layer Receptivity for Blunt Compression-Cones in Mach-6 Flow

Yuet Huang[1] and Xiaolin Zhong[2]
University of California, Los Angeles, California, 90095

This paper presents the direct numerical simulations (DNS) of transient flow under the effect of interaction between freestream hotspot perturbation and bow-shock on Purdue's blunt compression cones in Mach-6 freestream by using shock-fitting method. The flow conditions that are used in the simulations are the same as Boeing/AFOSR Mach-6 Quiet tunnel (BAM6QT) in Purdue University, and the comparison of the simulation results with Purdue's laser-spot wind-tunnel experiment results is expected. The geometric design of the blunt compression cones creates an adverse pressure gradient along the cone wall in streamwise direction, hence, the laminar-turbulence transition takes place at a shorter streamwise distance when comparing to the blunt straight-cones. The detailed analysis of the mechanisms of receptivity and instability are carried out based on the simulation results. Particularly, the instability of the second mode in boundary layer along the compression cone wall in streamwise direction is investigated.

Nomenclature

M_∞	=	freestream Mach number
ρ_∞	=	freestream density
T_o	=	total temperature
T_{wall}	=	temperature at the wall
γ	=	ratio of specific heat
Pr	=	Prantl number
R	=	gas constant
μ_r	=	reference viscosity coefficient
T_r	=	reference temperature
T_s	=	Sutherland's temperature
T_∞	=	freestream temperature
e	=	total energy per unit volume
q_j	=	heat flux due to thermal conduction
τ_{ij}	=	shear stress tensor
$\frac{\mathrm{Re}_\infty}{L}$	=	freestream Reynolds number per unit length

I. Introduction

In designing the future hypersonic aerospace vehicles, being able to predict the boundary layer laminar-turbulence transition location on the body plays an extremely important role on aerodynamic heating analysis. When the vehicle is travelling in atmosphere at hypersonic speed, there are weak disturbances exist in the freestream. The process for the freestream disturbances to cause laminar-turbulence transition can be divided into three stages: (i) boundary layer receptivity, (ii) linear eigenmode growth or transient growth, and (iii) nonlinear breakdown to turbulence [16]. Boundary layer receptivity is the process for the freestream disturbances enter the boundary layer and generate instability waves. And, boundary layer receptivity is a preliminary stage for laminar-turbulence transition to occur [2, 8].

Linear disturbance waves in hypersonic boundary layer contain normal modes. The unstable modes are found by Mack, and he has pointed out that the second mode is the dominant instability which leads to transition when Mach number is approximately higher than 4 [7, 19]. During the flight of hypersonic vehicle, the weak disturbances in

[1] Post-graduate Student, Mechanical and Aerospace Engineering Department.
[2] Professor, Mechanical and Aerospace Engineering Department, AIAA Associate Fellow.

freestream is analogical to the linear disturbance waves, thus the second mode instability is particularly important for study.

In hypersonic flow, the bow-shock in front of the blunt nose creates entropy and vorticity layers, which will be swallowed by the boundary layer in downstream [8]. The swallowing process of entropy layer has a strong effect on the boundary layer stability [7]. Thus, the second mode instability can be affected by the entropy layer swallowing process [7].

Kovasznay [11] stated that weak disturbances in compressible flow can be decomposed into acoustic, entropy and vorticity disturbance. McKenzie et al. [10] found that regardless of the type of disturbances, the behind-shock acoustic, entropy and vorticity disturbances would always be generated when it interacts with shock. However, the mechanisms of the interaction of various types of disturbance with the shock are individually different, which would lead to difference in travelling angle and amplitude of the generated disturbances. In nature, the disturbances exist in freestream during flight in atmosphere consist of all three kinds. Thus, detailed boundary layer receptivity studies of all three types of freestream disturbance and shock interaction are necessary for completely understanding the mechanism of hypersonic boundary layer receptivity over blunt body. Freestream acoustic disturbance receptivity has been studied much nowadays [3, 4], and using laser equipments to generate hotspot is a possible way for imposing freestream disturbances other than acoustic disturbance in a wind tunnel [3, 4]. These are the reasons for us to use hotspot as the freestream disturbance in this paper.

The simulations in this paper are cooperated with the experiments at Purdue University. The schematic explanation of the laser-spot (hotspot) and cone scenario is demonstrated in Figure 2. The hotspot is generated at some location upstream from the cone on the centerline. Then the spot convects with the hypersonic freestream toward the cone nose, and eventually interacts with and passes through the bow shock, and travels further downstream in shock layer. The goal of this paper is to study the effects of freestream hotspot perturbation to the growth of instability waves in boundary layer behind the shock.

Compression cone (see Figure 1) is a circular-base cone with circular-flared geometry along its body in downstream direction. Such geometry was expected to cause laminar-turbulence transition under quiet-flow condition due to adverse pressure gradient occurs along the flared geometry of the cone [5, 7]. The adverse pressure gradient is verified in Huang & Zhong's [13] mean flow DNS, see Figure 4. The aim of having such geometry is to make the boundary layer thickness remain constant in downstream direction, while a narrow range of instability frequencies can be continuously amplified [5].

In Huang & Zhong's [13] hotspot DNS study in 2010, the results indicate that the freestream entropy perturbation would generate entropy and acoustic disturbances after passing through the bow shock, and the acoustic disturbance behind shock would bounce back from the wall and interact with the bow shock again, and generate acoustic and entropy disturbances.

Ma & Zhong [16] stated that when the acoustic waves generated from freestream entropy perturbation and shock interaction, reaches the boundary layer, the perturbed boundary layer will reflect acoustic waves and transmit to interact with the shock again, and generate additional acoustic, entropy and vorticity disturbances. These additional disturbances combined with the initial disturbances and propagate downstream would produce strong effect on the receptivity. Ma & Zhong have also performed DNS study on flat plate with freestream sinusoidal entropy waves at Mach 4.5. They found that the receptivity of supersonic boundary layer to freestream entropy waves is essentially similar to the receptivity to freestream fast acoustic waves; the fast acoustic waves generated behind the shock and propagate downstream into the boundary layer, and excite the instability modes in it. Ma & Zhong has compared their simulation results with McKenzie et al.'s theoretical results, and have good agreement.

In 2010, Huang & Zhong [13] have completed mean flow DNS with shock-fitting method for a very blunt compression cone with nose radius of 0.0127m, and a sharper cone with nose radius of 0.001m. In order to validate the resulting mean flow, LST analysis was performed for the sharper cone mean flow, which gives N-factor = 12.5 with the most amplified frequency of 278996 Hz. Both LST and shock-front position results agree well with Purdue's shock-capturing DNS results. Huang & Zhong have also developed the computer program for simulating the three dimensional hotspot perturbed flow behind bow-shock. Huang & Zhong have validated the program with running a freestream sinusoidal entropy wave, and obtained a qualitatively correct stagnation line perturbation distribution. And Huang & Zhong have investigated the structure of the hotspot perturbation behind the bow-shock by computing two cases of freestream hotspots with very small radii (hotspot case B, C).

This paper is a continuation of the realistic sized hotspot case (hotspot case A) DNS from Huang & Zhong's 2010 paper [13]. Since in that paper, the main focus is on creating the mean flow results, development and validations of the hotspot perturbed flow simulation computer code. In this paper, the stages are: (i) simulation of the unsteady hotspot perturbed flow for the entire blunt compression cone, (ii) the detailed investigations on instability modes excitation of hotspot perturbed boundary layer, which is performed after the simulation is completed. Huang &

Zhong have already finished the simulation of hotspot perturbed flow in zone 1, which is at the hemispherical cone-nose region, see Figure 7 for the time history of the entropy perturbation on the stagnation line, Figure 8 is the time history of the pressure perturbation on the stagnation line, Figure 9 is the time history of entropy perturbation on the wall , Figure 10 is the time history of pressure perturbation on the wall, Figure 11 and 12 are the entropy and pressure contours of the hotspot perturbation.

II. Governing Equations and Numerical Methods

The governing equations for DNS of hypersonic perfect-gas flow around compression cone are the following three-dimensional Navier-Stokes equations in conservative-law form and Cartesian coordinates:

$$\frac{\partial U}{\partial t}+\frac{\partial F_j}{\partial x_j}+\frac{\partial F_{vj}}{\partial x_j}=0,\ \ j=1,2,3$$

The tensor notation, (x_1, x_2, x_3) represents the Cartesian coordinates, (x, y, z). x is the axis along the centerline of the cone, pointing in the direction from nose to bottom of the cone. y is the axis pointing vertically upward from the centerline of the cone, and it is perpendicular to the x axis. z is the axis perpendicular to both x and y axes, and it is pointing away from the centerline of the cone. The origin of the axes is at the center of origin of the spherical cone nose. Vector U contains five conservative-law form dimensional flow variables:

$$U=\begin{bmatrix}\rho & \rho u_1 & \rho u_2 & \rho u_3 & e\end{bmatrix}$$

F_j and F_{vj} are the vectors of convective (invicid) flux and viscous flux in jth spatial direction respectively:

$$F_j=\begin{bmatrix}\rho u_j\\ \rho u_1u_j+p\delta_{1j}\\ \rho u_2u_j+p\delta_{2j}\\ \rho u_3u_j+p\delta_{3j}\\ (e+p)u_j\end{bmatrix}$$

$$F_{vj}=\begin{bmatrix}0\\ -\tau_{1j}\\ -\tau_{2j}\\ -\tau_{3j}\\ -\tau_{jk}u_k-q_j\end{bmatrix},\ \ k=1,2,3$$

The equation of the state and the transport equations are:

$$p=\rho RT$$

$$e=\rho\left(c_vT+\frac{1}{2}u_ku_k\right)$$

$$\tau_{ij}=\mu\left(\frac{\partial u_i}{\partial x_j}+\frac{\partial u_j}{\partial x_i}\right)-\lambda\frac{\partial u_k}{\partial x_k}\delta_{ij},\ \ \lambda=\frac{2}{3}\mu$$

$$q_j = -\kappa \frac{\partial T}{\partial x_j}$$

where R is the gas constant, C_v is the specific heats that are assumed to be constant with a given specific heat ratio γ. κ is the heat conductivity coefficient, which can be determined with a constant Prantl number. The viscosity coefficient μ is defined by the Sutherland's law:

$$\mu = \mu_r \left(\frac{T}{T_0} \right)^{\frac{3}{2}} \left(\frac{T_r + T_s}{T + T_s} \right).$$

Throughout the numerical methods implementation in DNS of hypersonic flow around the blunt compression cone, the Cartesian Navier-Stoke's equations have been transformed into body-fitted curvilinear computational domain coordinates (ξ, η, ζ) via Jacobian matrix. The computational domain is bounded by the bow-shock and the wall of the cone, which is called 'shock-fitting' domain. Using shock-fitting method can accurately resolve the position of the bow-shock, which is necessary to obtain the high accuracy of the flow solutions for receptivity and stability analyses. The shock-fitting grids are moving-grids in time, and the motion is depended on the shock position and the shock velocity. See Figure 3 for a partial view of grid configuration. In each time-step, shock position and shock velocity are the unknowns, and would be solved by the freestream conditions and behind-shock solutions. Spatial discretization of inviscid flux derivatives in stream-wise (ξ) and wall-normal (η) directions are done by using fifth-order finite-difference upwind schemes with local Lax-Friedrichs flux-splitting scheme, and sixth-order central finite-difference scheme is used for viscous flux spatial derivatives. For spatial derivatives in periodic azimuthal direction (ζ), Fourier collocation method has been used. Runge-Kutta method is used for time-marching. The details of shock-fitting method, finite difference schemes and other numerical method implementations of the DNS are explained in Zhong's paper [6].

III. Modeling Equations of Freestream Hotspot Perturbation

Physically a hotspot is an entropy perturbation sphere with acoustic perturbation (weak shock) surrounds it. The entropy core has Gaussian temperature or density distribution [3, 4]. Same as in Huang & Zhong's paper [13] in 2010, consider if the hotspot is relatively large compare to the cone nose, then the influence from the acoustic weak shock is very small, and the entropy effect is the essence, therefore, here the hotspot is modeled without weak shock surrounds it. Since the initial position of the hotspot is 2cm upstream from the shock on centerline in Dunn's paper [1], the time scale for the hotspot to diffuse and propagate in freestream is very small when comparing to the length scale of the initial distance between center of hotspot and shock-front on centerline. Hence, it is reasonable to assume the hotspot profile remains unchanged when convecting with freestream.

For 3D hotspot model, the Gaussian perturbed freestream temperature is:

$$T = \Delta T_{\max} \exp\left(-\frac{R_c^{\,2}}{2\sigma^2} \right) + T_\infty,$$

thus, by ideal gas law, the perturbed freestream density is:

$$\rho = \frac{p_\infty}{R\left(T_{\max} \exp\left(-\frac{R_c^{\,2}}{2\sigma^2} \right) + T_\infty \right)},$$

the time derivative of perturbed freestream density at shock location is:

$$\frac{\partial \rho}{\partial \tau} = \left(\frac{p_\infty}{\sigma^2 R} \right) T^{-2} \left(T - T_\infty \right) \left[\left(X_c - U_\infty t \right) \left(\frac{\partial X_c}{\partial \tau} - U_\infty \right) + y_{shk} \frac{\partial y_{shk}}{\partial \tau} + z_{shk} \frac{\partial z_{shk}}{\partial \tau} \right],$$

where σ is Gaussian shaping factor, τ is time in computational domain. X_{spot} is the initial x-coordinate of spot center. The initial x-coordinate difference between the shock location and the spot center is:

$$X_c = \left| X_{spot} - x_{shk} \right|,$$

x_{shk}, y_{shk}, z_{shk} are shock-front coordinates. By using the transport equation in mathematics, the distance between hotspot center and any point on the shock front at any time is:

$$R_c = \sqrt{\left(X_c - U_\infty t\right)^2 + y_{shk}^2 + z_{shk}^2}\,.$$

Please note that the time in computational domain is the same as the time in physical domain [6].

IV. Boundary Layer Instability Spectral Analysis

The hotspot simulation is performed based on the converged mean flow. The temporally varying boundary layer flow variables while the hotspot is passing by the mean flow are recorded at a sufficient temporal well-resolved rate. However, the recorded boundary layer flow perturbation is a combination of infinite frequency components. In this study, the main interest is to see which frequency would excite instability in boundary layer and how fast is the instability growing spatially. Therefore, it is necessary to have the time-history of the boundary layer perturbation transform into frequency domain, in order to see the behavior of different frequency components. The mathematical method that is used in the instability analysis is Fourier transformation. By definition, continuous Fourier transformation of a flow variable *h(t)* is defined as[20]:

$$H(f) = \int_{-\infty}^{\infty} h(t) e^{2\pi i f t} dt$$

where *h(t)* is the flow variable time function, *H(f)* is its spectral value in frequency domain. Numerically, the continuous Fourier transformed spectral value can be approximated by:

$$H(f_n) \approx \Delta t \sum_{k=0}^{N-1} h_k e^{\frac{2\pi i k n}{N}}$$

where $H(f_n)$ is the spectral value at nth discretized frequency, N is the total number of Fourier collocation points used to discretize the time function, *h(t)*. The discretized time function is h_k. The spectral value, *H(f)*, has real and imaginary components in frequency domain. The $|H(f)|$ is the magnitude of the real part and the imaginary part of *H(f)*. In this paper, *h(t)* is the time-history of boundary layer perturbation, and the *H(f)* is the spectral value of the boundary layer perturbation in frequency domain.

After obtaining the frequency component of the boundary layer, it is necessary to validate the results of the DNS. Here, the comparison with LST is chosen as a method to prove the validity of DNS. In other papers, such as Zhong [7] and Sivasubramanian [21], the common practice is to compare the local spatial growth rate, local wave number, and the wall-normal boundary layer mode shape with LST.

Local growth rate in linear stability theory (LST) is defined as [19]:

$$\alpha_i = \frac{1}{\left|H(f_n)\right|} \frac{d\left|H(f_n)\right|}{ds}$$

where s is the natural coordinate along the body surface. Local wave number in LST is defined as [19]:

$$\alpha_r = \frac{d\varphi_n}{ds}$$

where φ_n is the phase angle of *H(f)* at nth discretized frequency. The wall-normal mode shape is the spatial distribution of the Fourier transformed spectral value, *H(f)*, along the normal of cone surface.

V. Freestream Conditions and Compression Cone Geometries

The freestream conditions used in the numerical simulations in this paper is based on Purdue's Mach-6 Quiet Tunnel (BAM6QT) [5]:

$M_\infty = 6.0$
$\rho_\infty = 0.0403\ kg/m^3$
$T_o = 433.0\ K$
$T_{wall} = 300.0\ K$
$\gamma = 1.4$
$Pr = 0.72$
$R = 287.04\ Nm/kgK\ (air)$
$\mu_r = 1.7894 \times 10^{-5}\ kg/ms\ (sea\ level)$
$T_r = 288\ K\ (sea\ level)$
$T_s = 110.3333K\ (air)$
$\frac{\mathrm{Re}_\infty}{L} = 1.026 \times 10^7\ m^{-1}$

The compression cone geometry is based on Schneider's design [5]:

body-arc radius = 3.0 *m*
cone half-angle = 2.0 *degrees*
cone length $\approx$ 0.45 *m*
nose radius = 0.001 *m* (Purdue's)

Since the flow conditions and cone geometry are based on Purdue's experiment, our simulation results can be compared with his wind tunnel experiment results. The nose radius is the same nose radius used in case 2 in Huang & Zhong [13].

VI. Freestream Hotspot Parameters

The peak radius is controlled by the Gaussian factor, σ. In Huang & Zhong [13]'s paper in 2010, there are three cases of different hotspot peak-region radius for DNS with hotspot perturbation. In this paper, the hotspot size is referred to the actual hotspot size in Purdue's experiments [3, 4], which is case A in Huang & Zhong [13].

σ = 0.001 (largest radius: r = 0.003 m), X_{spot} = -0.02 m

The hotspot perturbed flow simulation in this paper is based on the mean flow solution of case 2 in Huang & Zhong [13], and in order to keep the disturbance linear in the flow, the maximum temperature perturbation amplitude is chosen to be:

$$\Delta T_{\max} = T_\infty \times 10^{-4} = 0.00528K.$$

The profiles of the freestream temperature and density distribution in radial-direction within a modeled 3D hotspot are demonstrated in Figure 5 and 6.

VII. Procedures and Simulation Results

Unless mentioned specifically, all flow variables shown in the figures are dimensionless, which are normalized by the corresponding freestream values. For all contour plots, the upper boundary is the location of the shock, the lower boundary is the cone-wall, the left boundary is the flow inlet, and the right boundary is the flow exit. Since the cone is at zero degree angle of attack, only the upper half of the cone is demonstrated, and the lower half is the mirror image of the upper half due to axis-symmetry of the flow. Figure 3 shows the partial view of the computational grid structure around the cone. Due to the limiting computer power for computing almost a million grid points at once, the simulation is divided into 18 zones. Zone 1 is the computation domain that wraps around the hemispherical cone nose, zone 2 to zone 18 wrap around the compression wall of the cone.

A. Unsteady flow Solution with Hotspot Perturbation in Freestream

The computation of zone 2 is using the exit boundary time history of zone 1 as the unsteady inlet boundary condition for zone 2 and the freestream perturbation at shock location as the perturbed shock boundary condition. While computing zone 1, the exit boundary condition is saved for every 10000 time steps. In zone 2 computation, the discrete time history of zone 1 exit boundary condition are interpolated by using 5^{th} order polynomials. The spatial resolution for zone 2 to zone 5 is $120 \times 120 \times 4$. Begin from zone 13, x=0.17m, the resolution in wall-normal direction has been doubled, since the flow become very unstable, which the flow field become very sensitive so that a small numerical error will be amplified and lead to erroneous results.

Figure 11 to 38 show the snapshots of entropy and pressure contours of the hotspot perturbation at various locations throughout the entire cone, passing through the inlet boundary at the left-hand-side, and convecting to the right, which is the downstream direction.

Zone 2 is the first zone behind the spherical cone nose, thus the effect of steep change in geometry is dominant in this zone. If one can see the motional pictures, the pressure perturbation hits the shock and reflects back towards the wall. Such phenomenon is called acoustic effect. However, this reflection phenomenon is not revealed in entropy perturbation. In zone 5, part of the boundary layer entropy perturbation travels ahead of the main body of the hotspot outside the boundary layer. The rear part of the entropy is elongated; this may due to the viscous effect in boundary layer that causes part of the boundary layer perturbation travels slower than the main body of the hotspot. The pressure perturbation has positive amplitude appears near the wall; this may due to the reflection of the acoustic perturbation from the wall, which is the acoustic effect. Zone 9 spans a longer streamwise distance, thus the typical structure of hotspot in upstream part of the cone and its spatial evolution can be clearly demonstrated. The entropy perturbation that is ahead of the main hotspot body in previous zones travels even farther ahead of it. And, the rear part of the entropy perturbation also become longer and longer, eventually formed a tail and broke apart from the main body of hotspot. The overall intensity of the entropy perturbation decays while travelling towards downstream. The pressure perturbation has acoustic wave in front of and behind the main body of hotspot. These waves could be the fast acoustic wave and slow acoustic wave respectively. There are only decaying waves appeared, the modes that are contained in the perturbation by zone 9 are spatially stable. Zone 12 is the zone right before the 'sensitive' region. 'Sensitive' means a small perturbation here can easily trigger the instability of the flow. The entropy perturbation has essentially two parts here, the main body and the first tail (in downstream, there will be another tail appeared). The boundary layer perturbations that travel ahead of the main body has been attenuated and become insignificant in zone 12. The pressure perturbation has two parts: the front part and the rear part. The front part is essentially the acoustic wave travels faster than the hotspot main body, and the rear part is essentially the acoustic wave that travels slower than the main body. Especially in the boundary layer, there are oscillations appear like some kinds of mode for both front and rear parts. In zone 14, the intensity of the hotspot main body has decayed so much, so that the intensity of the first tail becomes significant. And, the first tail becomes oscillatory. The pressure perturbation just keeps on decaying, and no growth or new mode is visible in zone 14. In zone 17, the first tail in entropy perturbation is oscillatory; it could be a kind of neutral mode, since it does not seem decaying. The second tail appears, and the intensity grows vigorously by travelling further downstream. In pressure perturbation, the front part and the rear part of the main body is growing slowly. And, a spatially unstable tail appears. The tail appears in oscillatory form. It is the unstable second mode, which will be verified in the second half of this paper. In zone 18, the main body of hotspot entropy perturbation keeps attenuating. The first tail grows at a slower rate than the second tail. The second tail grows to a level that dominates the perturbation. The first tail seems like a connection mode between the stable main body and the unstable second tail. In pressure perturbation of zone 18, the main body, which consists of front and rear parts, becomes subdominant while the tail grows to a level that exceeds the main body of hotspot pressure perturbation in zone 18.

From the pressure and entropy contours for all displayed zones, one can see that the intensity of hotspot perturbation outside of the boundary layer is decaying while the hotspot is moving downstream. Some of the boundary layer entropy perturbation travels ahead of the hotspot center that is above the boundary layer. A tail appears behind the both hotspot pressure and entropy perturbations and elongates while travelling further downstream. Such evolution of the perturbation in boundary layer is due to different wave modes exist in the boundary layer perturbations. In further downstream, the intensity of pressure perturbation grows at the elongated tail. The overall intensity of entropy perturbation does not seem to grow as vigorous as the pressure perturbation in downstream. Figure 29, 32, 35 and 38 are the entropy and pressure wall perturbation contour plots to demonstrate the second mode wave at the elongated tail in further downstream. Please note the small pressure oscillation at the tail that is right above the wall, it is the second mode perturbation, which grows and becomes unstable as travelling further downstream.

The upper left plot in Figure 40 is the wall pressure perturbation time-history profile of a laser spot near stagnation point of a hemispherical nose in a Mach 4 wind tunnel experiment by Randall [22, 28]. The upper right plot in Figure 40 is the DNS hotspot wall pressure perturbation time-history profile at x=0.0135m, which is about 3% of the total cone length. The lower left plot in Figure 40 is the DNS hotspot wall perturbation time-history profile at x=0.17m, which is about 38% of the total cone length. One can see that the hotspot profile at 3% of the total cone length that is quite close to the cone nose, the shape of the hotspot profile has not been altered too much due to the evolution of different wave modes in boundary layer. Such shape is quite comparable to the noise filtered shape of the experimental measured laser spot. The difference is that the weak acoustic shock effect at both ends exists in the experimental laser spot, but not included in the hotspot in DNS. From the time-history profile at 38% of the cone length, one can see the wave modes evolution has altered the shape, but the growth of second mode has not been encountered yet. Such shape is qualitatively similar to the original noise unfiltered wall pressure perturbation profile measured in the wind tunnel experiment. Again, the difference is the acoustic weak shock effect is included in the experiment, but excluded in DNS.

The local relative error of numerical convergence of the mean flow is controlled to be $O(10^{-9})$ in DNS. Figure 39 shows the ratio of amplitude of pressure wall-perturbation to the corresponding local mean flow pressure at x=0.313m. One can see that the amplitude to local mean flow ratio is $O(10^{-7})$. The local relative error is two orders of tenth power below the wall-perturbation ratio. Therefore, the boundary layer perturbation is not contaminated by the numerical convergence error.

B. Boundary Layer Receptivity Analysis

The wall pressure perturbation evolution on the compression cone is recorded in time at various spatial locations in downstream direction. Figure 41 and Figure 42 are the plots of the time-history traces, and the wall pressure perturbation amplitude is the relative value to the freestream pressure. One can notice in Figure 41, the perturbation time-history profile begins with a relatively monotonic shape consists of a main peak and a lower peak, both peaks could be fast acoustic wave and slow acoustic wave, and they gradually decay as travelling downstream, and split into multi-peak shape. Such evolution may due to the energy shift from one wave mode to another, which could be a result to the viscous effect of boundary layer. In Figure 42, the multi-peak perturbation begins to split into two parts in time; one with more oscillatory profile and the other part is smoother. As it travel further downstream, the perturbation amplitude decays, and both parts depart from each other in time. Both parts are probably different wave modes, since they have totally different perturbation profile, and they travel with different velocities; the more oscillatory part travels faster than the smoother part. When moving further downstream, another new perturbation mode appears and its amplitude grow so vigorously as moving downstream and soon the new mode amplitude surpasses the original decaying modes and become the dominant instability in boundary layer. This new mode is the second mode instability, it appears in the time-history profile around x=0.25m, which is 56% of the total cone length.

Figure 43 shows the spectrum of wall pressure perturbation with a wide range of frequencies at various streamwise locations. Please note the color of the curve lines, they represents different streamwise locations. The plot clearly shows that there is a spatial growing amplitude peak at the frequency range from about 260 kHz to 320 kHz. And the peak to the left of the growing peak, at the frequency range from 190 kHz to 260 kHz, is not decaying nor growing spatially. That peak could be the first mode at lower frequencies. Figure 44 shows the development of the wall pressure perturbation spectra in streamwise direction. Please note that the amplitudes of the spectra are plotted in logarithmic scale.

Figure 45 and Figure 46 are the LST analysis results that are completed in Huang & Zhong's paper in 2010 [13]. LST analysis has predicted the second mode frequency range, and it is represented by five proposed frequencies; 257498 Hz, 271797 Hz, 278996 Hz, 292494 Hz and 297494 Hz. Since the LST proposed 2nd mode frequency range is matching with the growing peak frequency range in DNS, the growing peak is concluded to be the second mode instability. In order to compare the DNS results with LST results, the sampling frequencies which are the closest to the five proposed frequencies are selected and to be investigated. According to the LST results, the most amplified frequency amongst the five proposed ones is 278996 Hz, the second most amplified frequency is 292494 Hz at any location between x=0.3m to 0.4m.

In Figure 44, five 2nd mode sampling frequencies that are the closest available sampling frequency to the five LST proposed frequencies are investigated. The most amplified sampling frequency is 292900 Hz, and the second most amplified sampling frequency is 279750 Hz at x~0.35m. The five sampling 2nd mode frequencies amplitudes start growing at x~0.2m, and seemed growing linearly in tenth power at downstream locations. The least amplified frequency is 257222 Hz, and its curve is oscillatory that may due to multi-wave-modes interactions. Therefore, only the four most amplified 2nd mode sampling frequencies are further analyzed.

Comparisons between the DNS spatial growth rates and the LST predicted spatial growth rates are demonstrated in Figure 47. Please note that the LST results are represented by the circular symbols, and the DNS results are represented by the lines. The oscillatory values at upstream is due to the unsmooth behavior in the spectral amplitude before the perturbations grow. The values become smoother shortly after the second mode growth occurs at downstream locations. The growth rates of the 2nd mode sampling frequencies are consistently comparable to the LST at downstream. The difference between the DNS growth rates and the LST growth rates is consistently about 10% at downstream. The reason for this consistent difference to occur is most likely due to non-parallel effect in LST analysis.

In order to further validate the DNS results, the comparisons between less non-parallel effect sensitive values are necessary [21]. Figure 48 is the comparisons between the DNS wave numbers and the LST wave numbers for the four most amplified 2nd mode sampling frequencies. Please note that the LST results are represented by the circular symbols, and the DNS results are represented by the lines. The oscillation in the lines are due to the numerical noise, however, it does not contaminate the values of wave numbers. One can see that the DNS wave number is very agreeable with the LST wave number at downstream. The most deviant case is the case with the 2nd mode sampling frequency of 272250Hz, the different between the DNS wave number and the LST wave number is about 1%. The case with 296650Hz is excellently matched with LST wave number at downstream locations.

Figure 49 shows the comparison between the DNS wall-normal boundary layer perturbation mode shape with the most amplified 2nd mode sampling frequency of 292900Hz to the LST mode shape within boundary layer. The comparison indicates high degree of agreement between DNS and LST mode shape. From the above agreements from the three different comparisons, it can be concludes that the DNS captures the linear development of hotspot boundary layer perturbation in a manner of high accuracy, and the resolution is sufficient.

VIII. Conclusion

In this paper, we have completed the unsteady simulation of hotspot perturbed shock layer on Purdue's compression cone under Mach-6 freestream by solving the full Navier-Stokes equations. The overall structures of the hotspot perturbation have been thoroughly studied at various streamwise locations in the shock layer, and some modal behaviors have been observed. The profile of the hotspot perturbation in boundary layer has been compared with the laser spot profile measured in Purdue's experiment at earlier time [22, 28]. The hotspot boundary layer perturbation profile is qualitatively comparable with the experimental hotspot profile, except the acoustic weak shock wave effect is not assumed in this simulation.

The boundary layer receptivity analysis based on the DNS results in presented in the second half of this paper. The spatial evolution of the time-history of the pressure perturbation in boundary layer is investigated. Particularly, the modal behavior in the boundary layer perturbation is observed. It has been found that there exists a new mode which grows dominantly in downstream. The spectrum of wall perturbation has been carried out. The dominantly growing mode frequency range is matching with the LST prediction of second mode that has been carried out in Huang & Zhong's previous paper [13]. Therefore, the new dominantly growing mode is concluded to be the second mode. The spatial behavior of the second mode instability growth is studied. The most amplified 2nd mode DNS sampling frequency is 292900 Hz, and the second most amplified DNS sampling frequency is 279750 Hz at x~0.35m. The least amplified 2nd mode DNS sampling frequency is 257222 Hz The second mode instability start growing at x~0.2m. Spectral validations of the DNS results with LST results have been completed. The well-agreements between DNS spectral results and LST results conclude that the DNS captures the linear development of hotspot boundary layer perturbation in a manner of high accuracy, and the spatial and temporal resolutions are sufficient.

Appendix

Unless mentioned specifically, all flow variables shown in the figures are dimensionless, which are normalized by the corresponding freestream values.

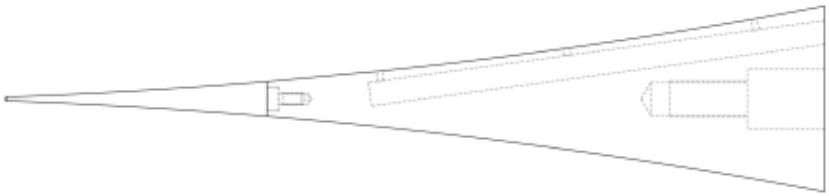

Figure 1. Schematic diagram of Purdue's Compression Cone [5]

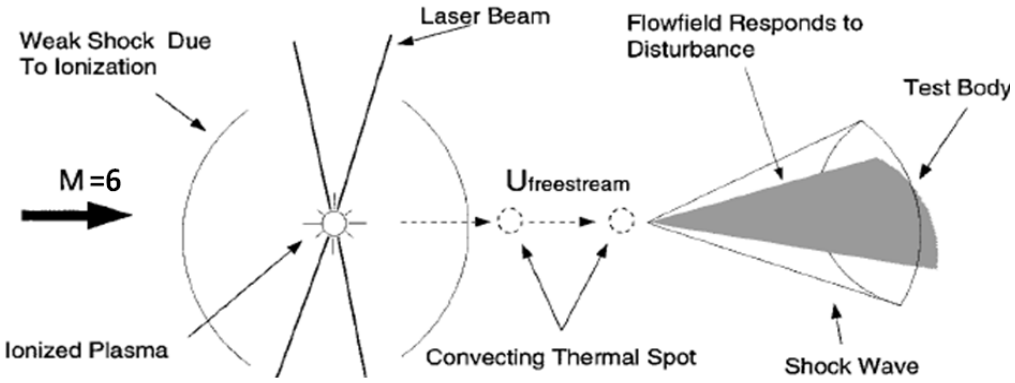

Figure 2. Schematic explanation of the laser-spot and cone scenario. [9]

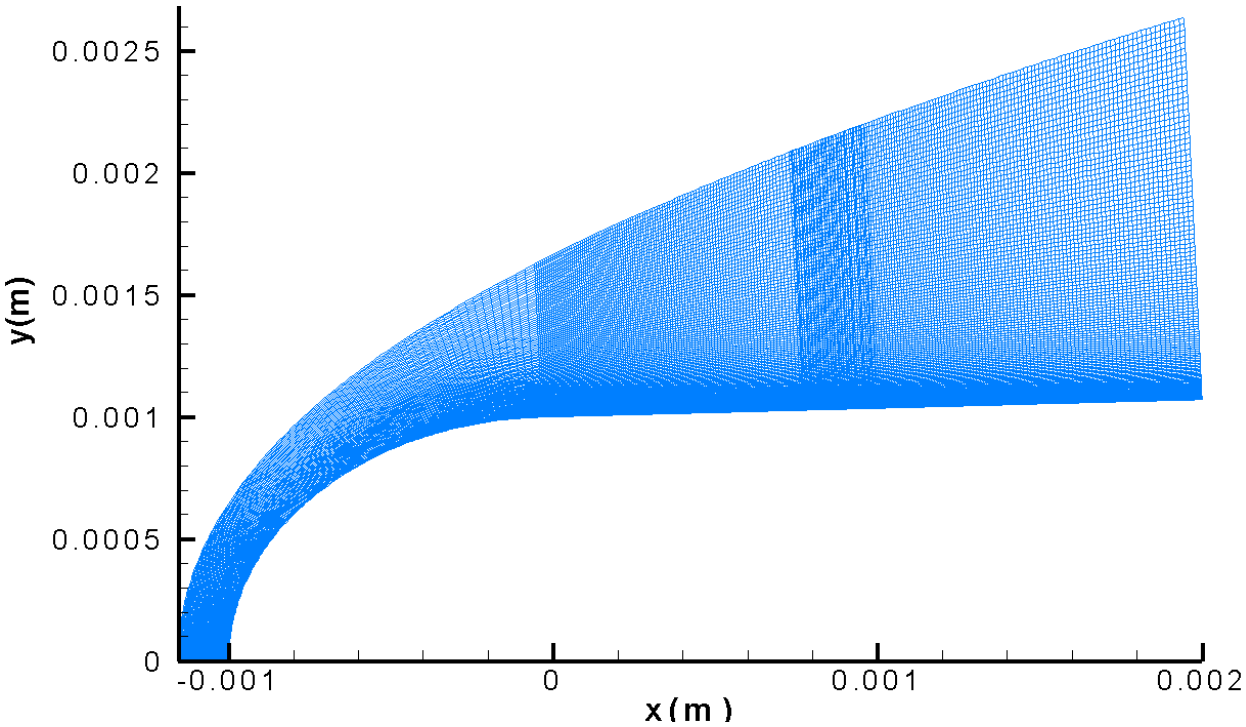

Figure 3. Partial view of grid configuration in zone 1, 2&3.

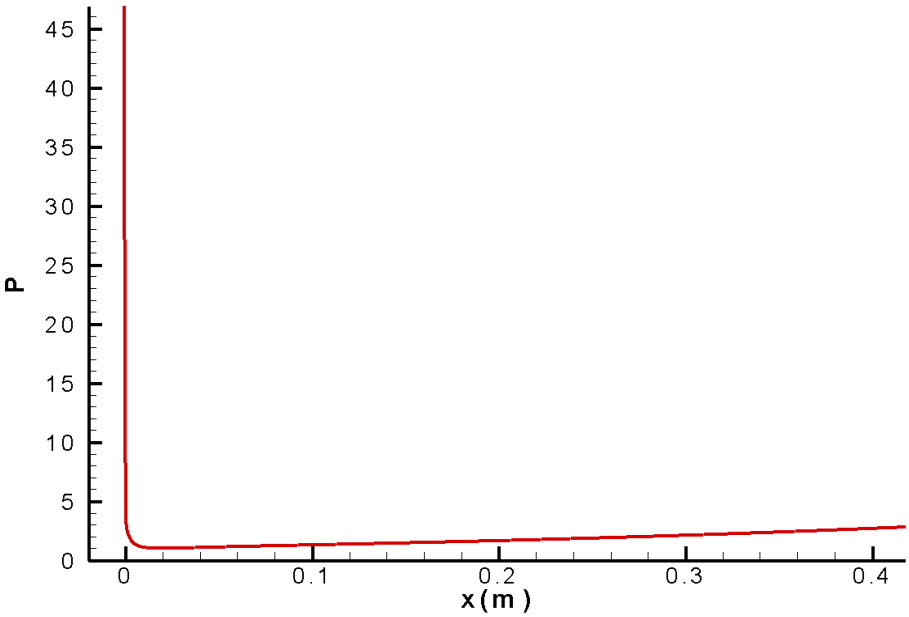

Figure 4. Pressure along the wall in case 2. [13]

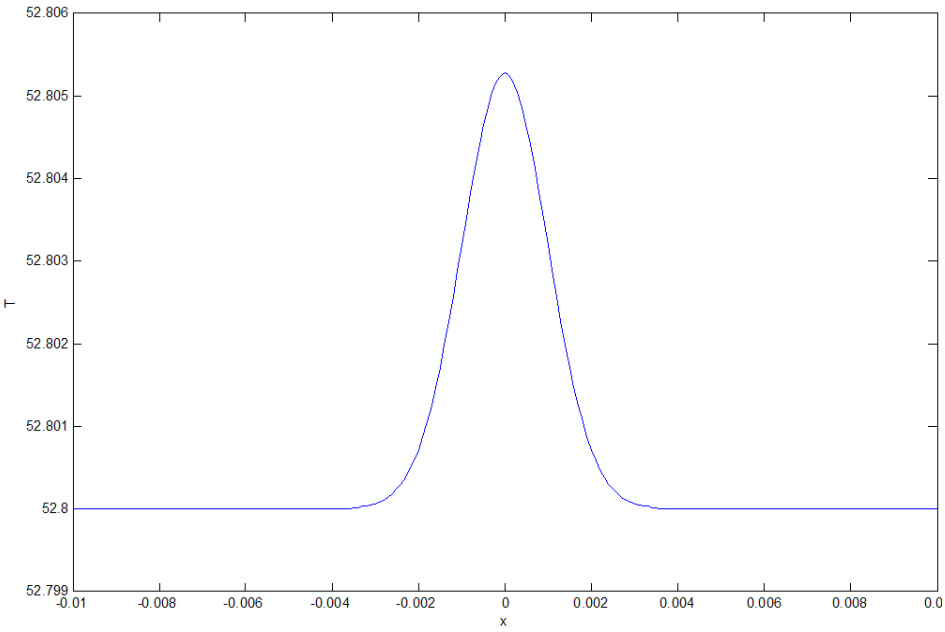

Note: x is radius in meter, T is temperature in degree Kelvin.

Figure 5. Gaussian distribution of perturbed temperature in radial-direction

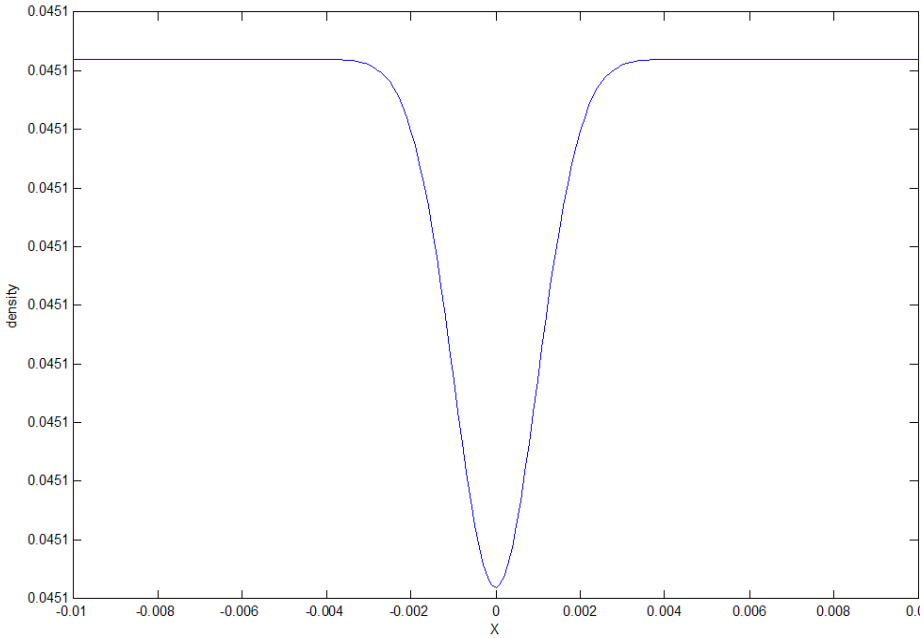

Note: x is radius in meter, density is in kg/m^3.

Figure 6. Gaussian distribution of perturbed density in radial-direction

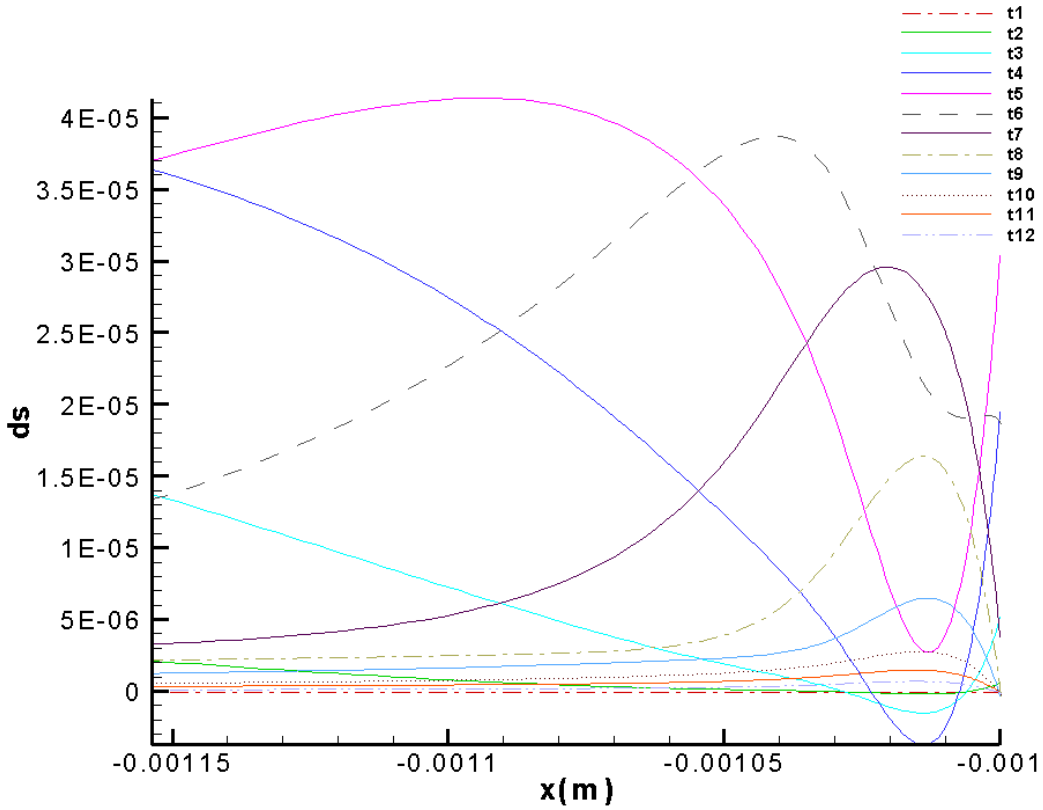

Figure 7. Entropy perturbation on stagnation line behind the shock at various time (case A, zone 1). [13]

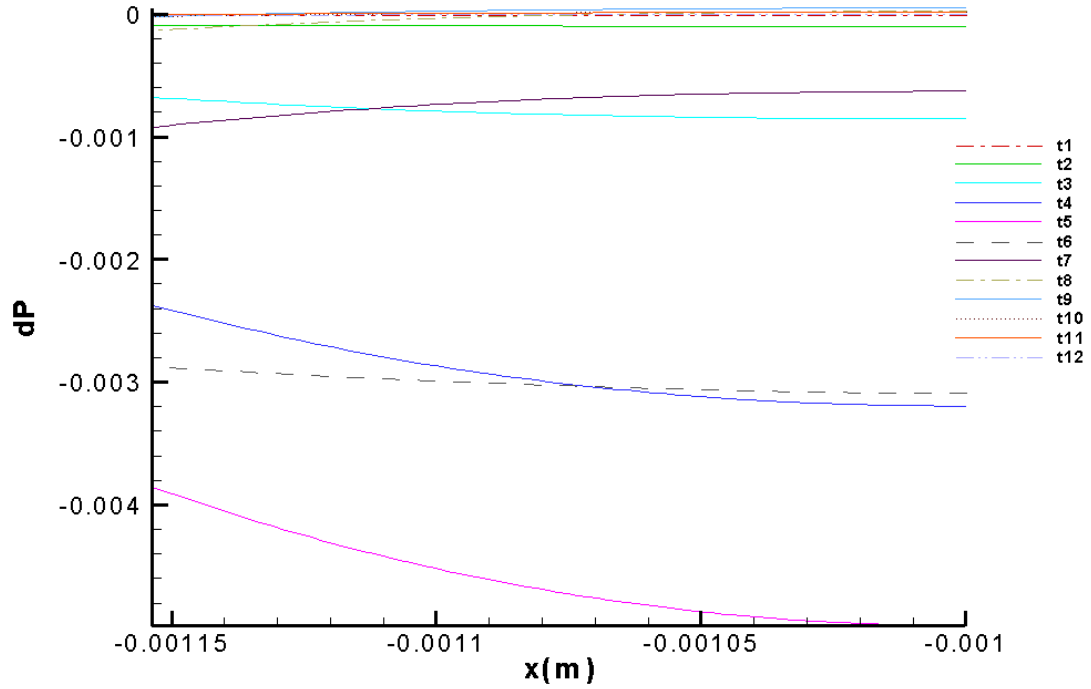

Figure 8. Pressure perturbation on stagnation line behind the shock at various time (case A, zone 1). [13]

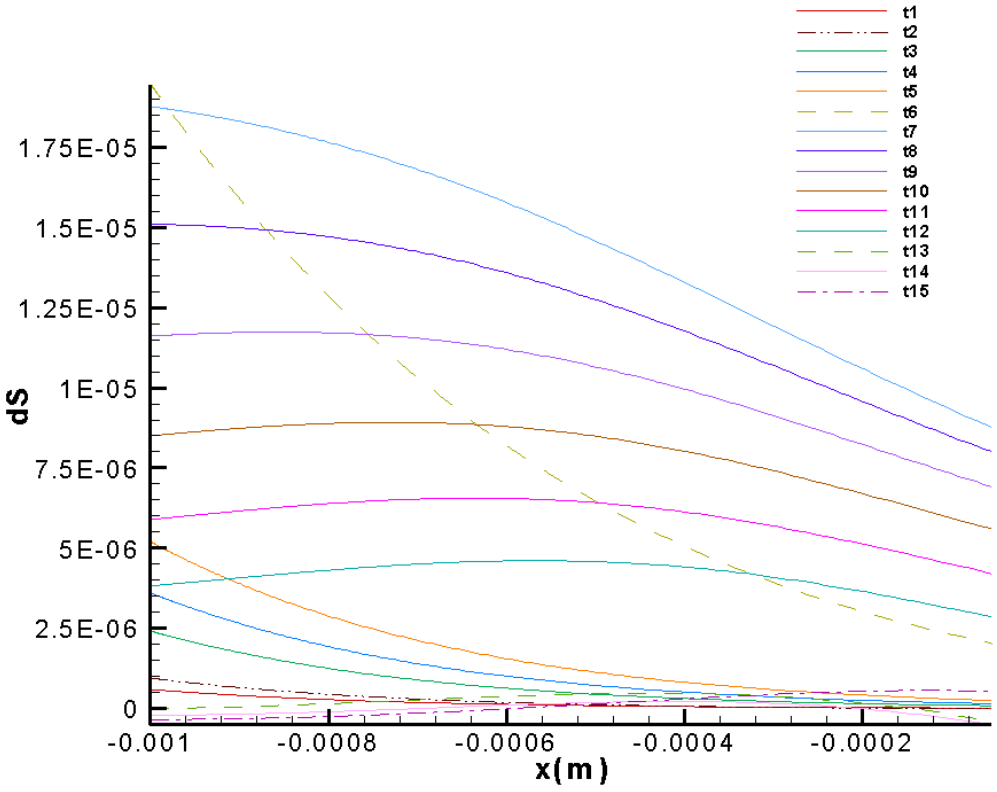

Figure 9. Entropy perturbation along wall surface at various time (case A, zone 1). [13]

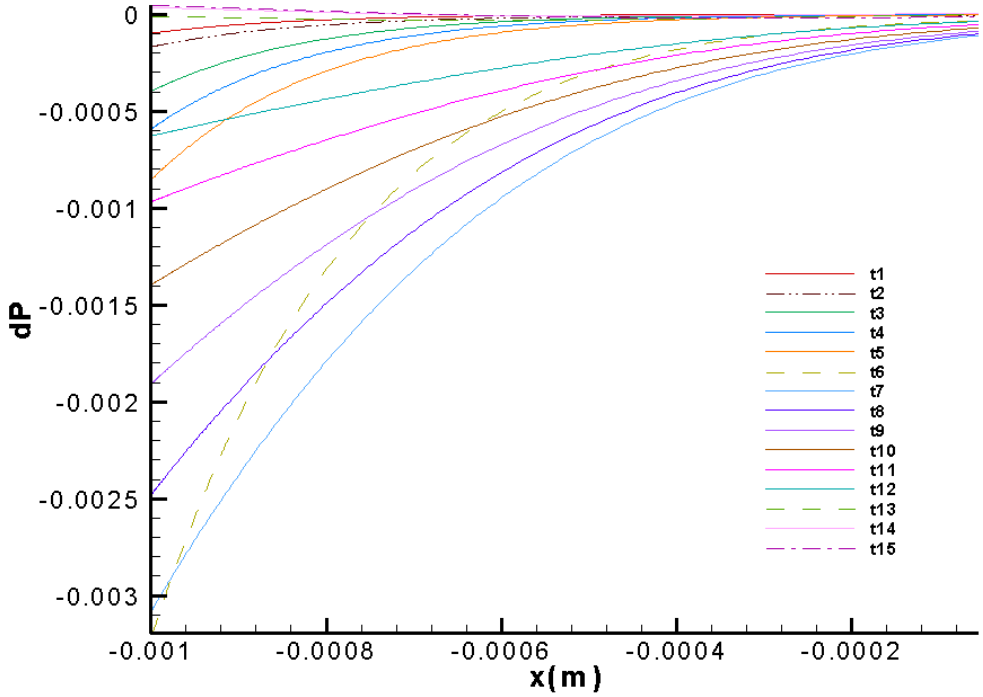

Figure 10. Pressure perturbation along wall surface at various time (case A, zone 1). [13]

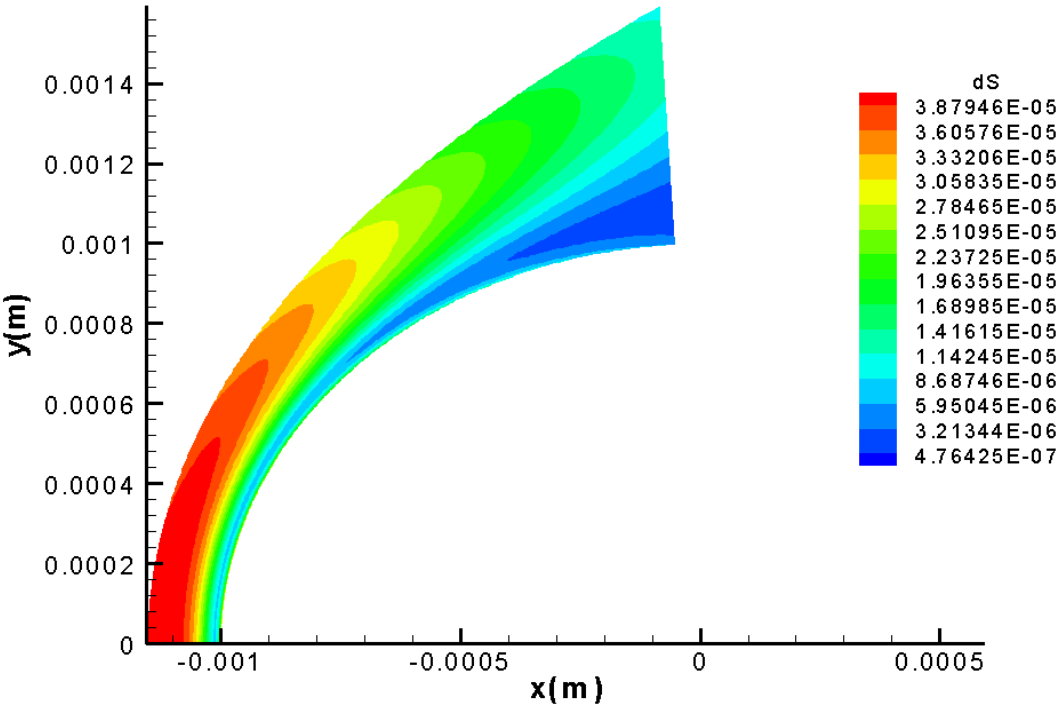

Figure 11. Contour plot of hotspot entropy perturbation behind the shock in case A, zone 1. [13]

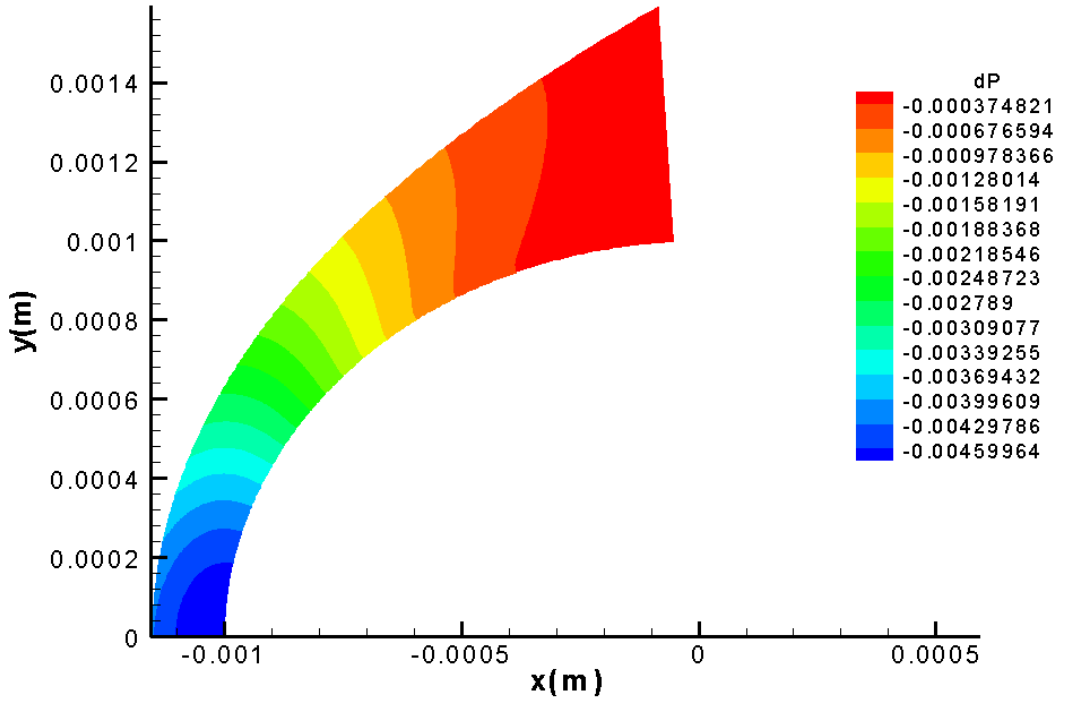

Figure 12. Contour plot of hotspot pressure perturbation behind the shock in case A, zone 1. [13]

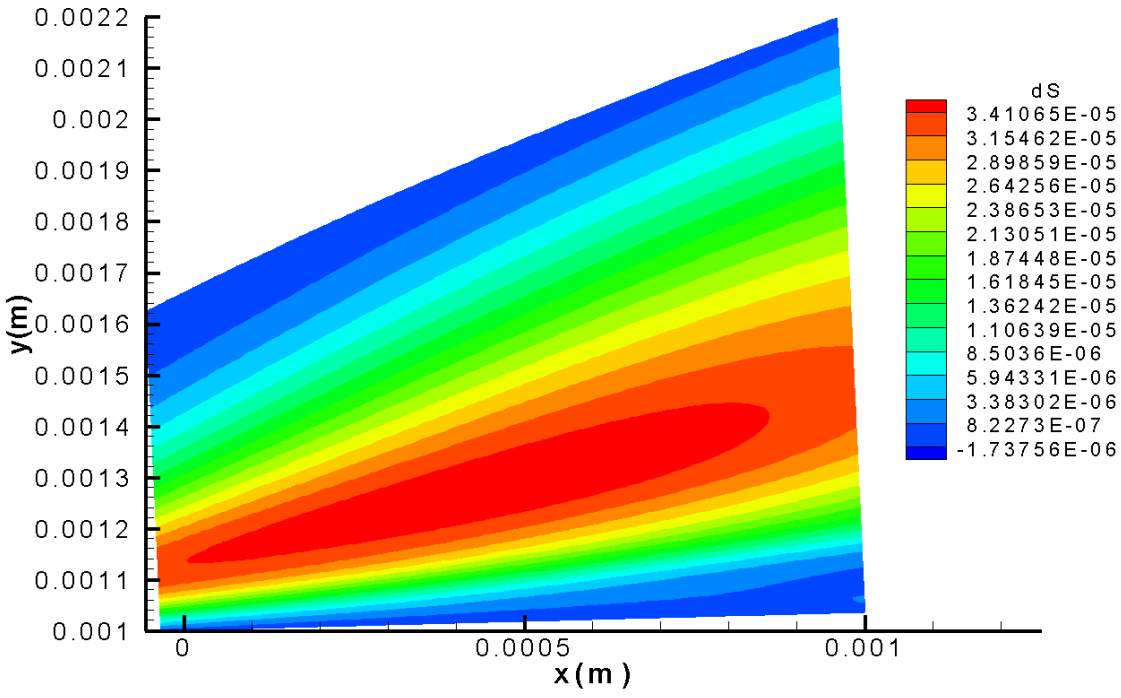

Figure 13. Contour plot of hotspot entropy perturbation behind the shock in zone 2

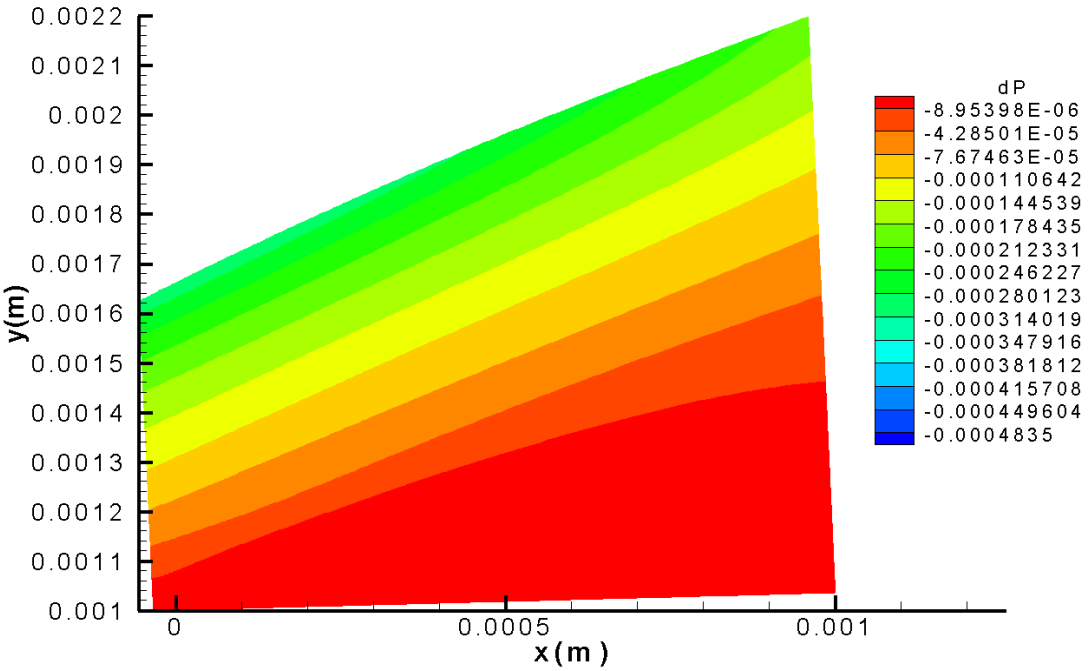

Figure 14. Contour plot of hotspot pressure perturbation behind the shock in zone 2

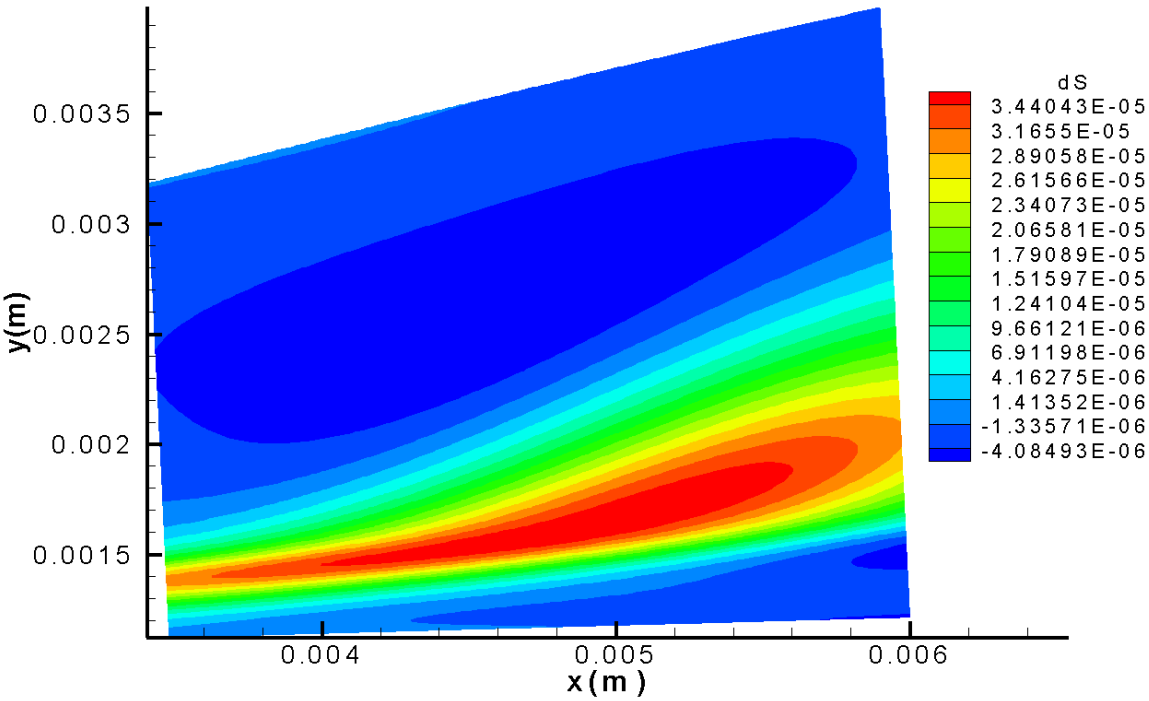

Figure 15. Contour plot of hotspot entropy perturbation behind the shock in zone 5

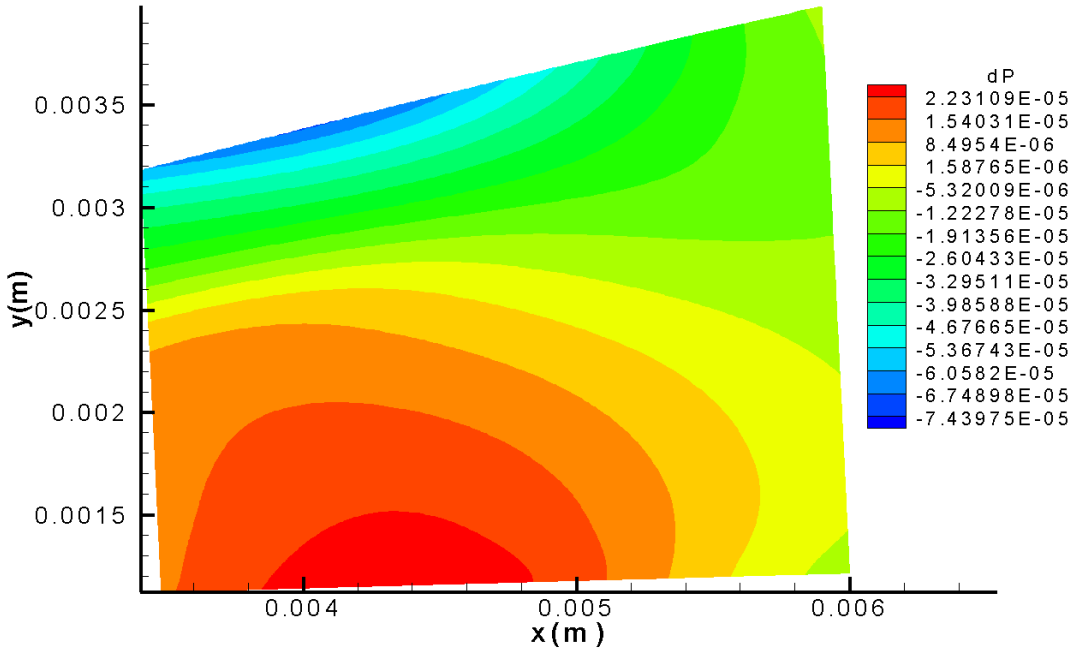

Figure 16. Contour plot of hotspot pressure perturbation behind the shock in zone 5

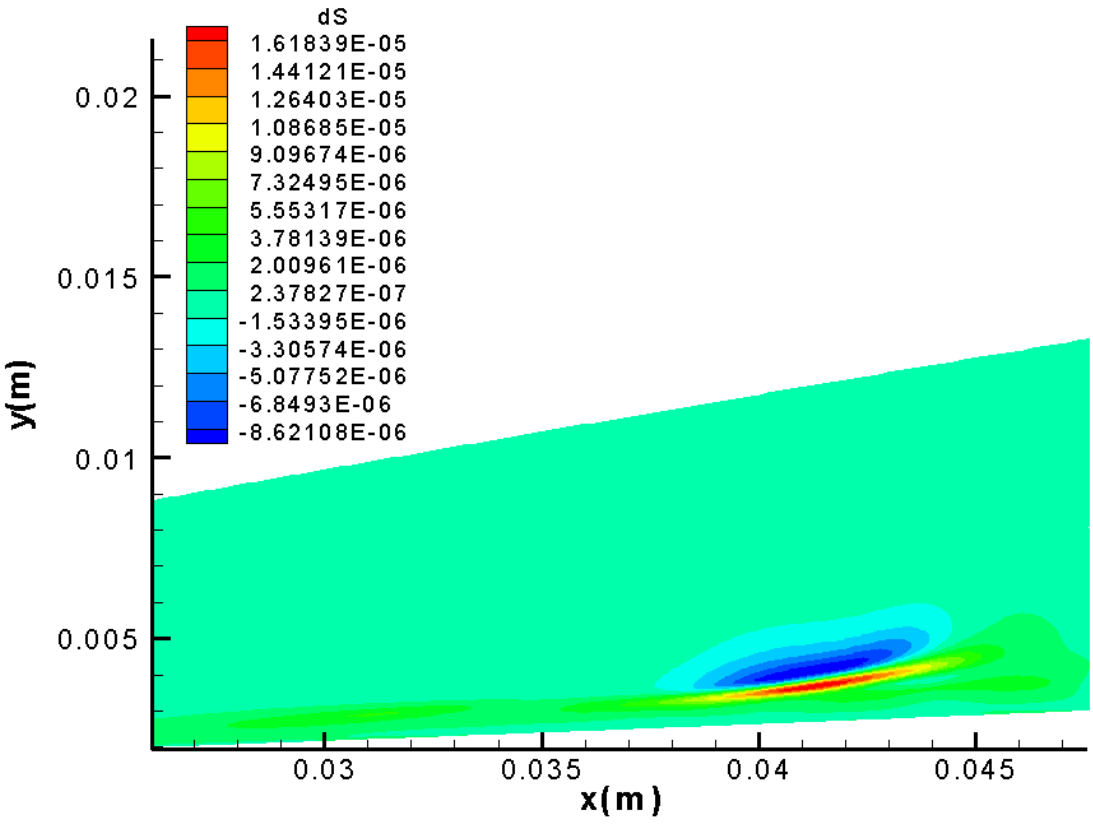

Figure 17. Contour plot of hotspot entropy perturbation behind the shock in zone 9

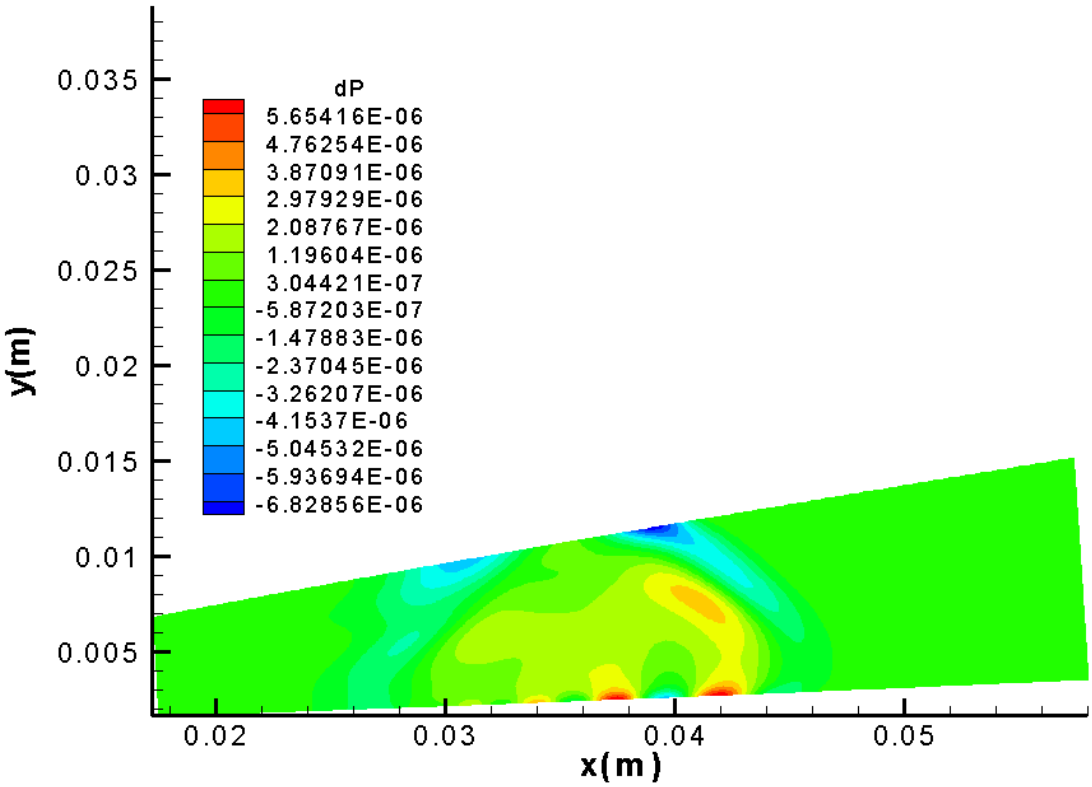

Figure 18. Contour plot of hotspot pressure perturbation behind the shock in zone 9

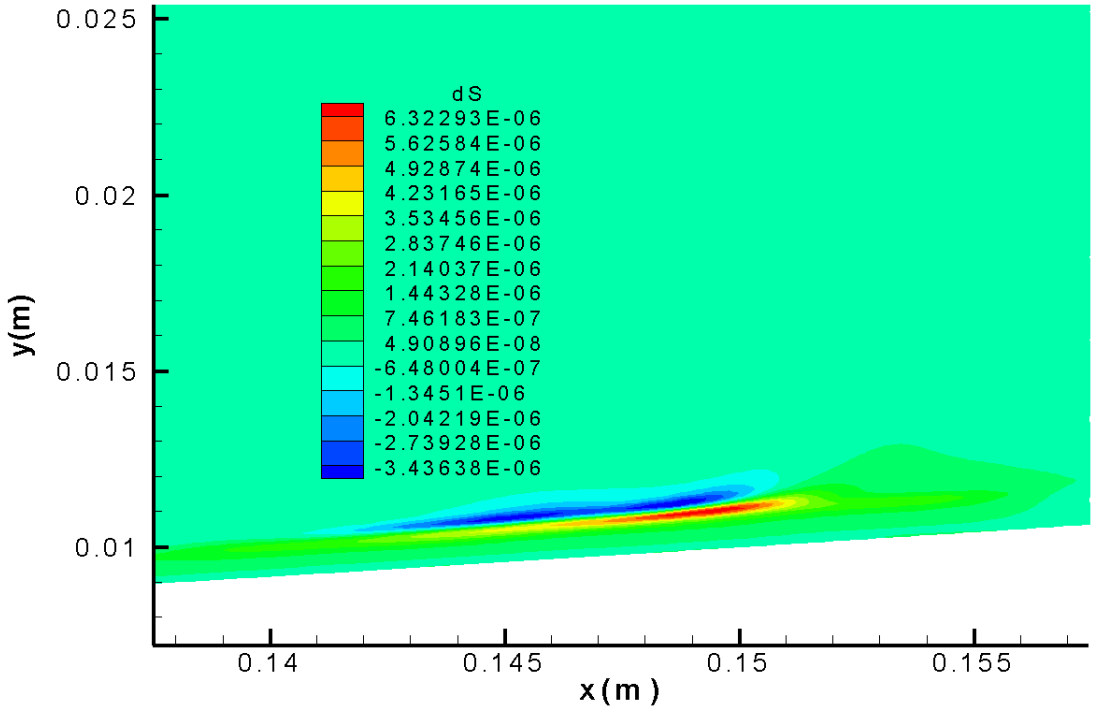

Figure 19. Contour plot of the main body of hotspot entropy perturbation behind the shock in zone 12

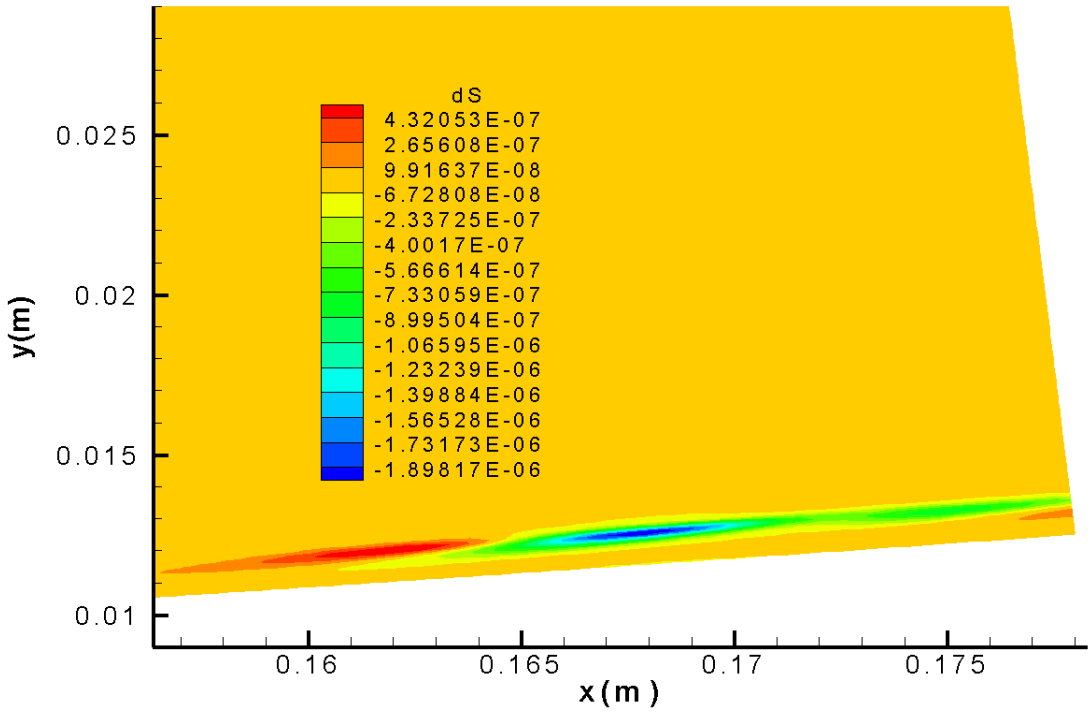

Figure 20. Contour plot of the first tail of hotspot entropy perturbation behind the shock in zone 12

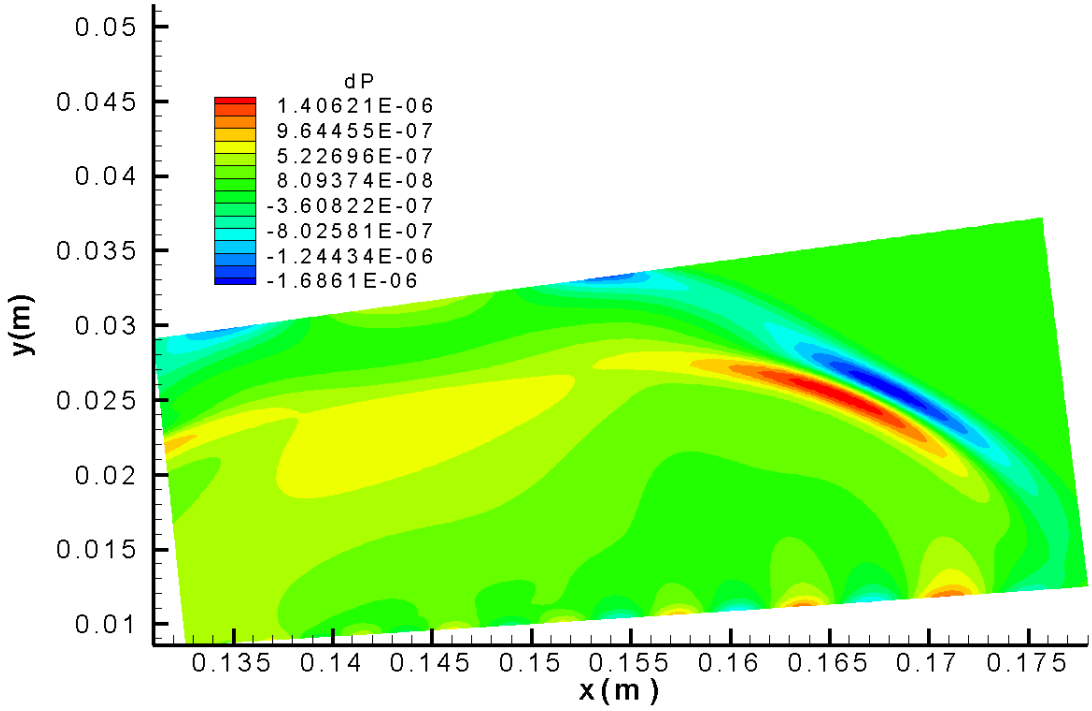

Figure 21. Contour plot of the front part of hotspot pressure perturbation behind the shock in zone 12

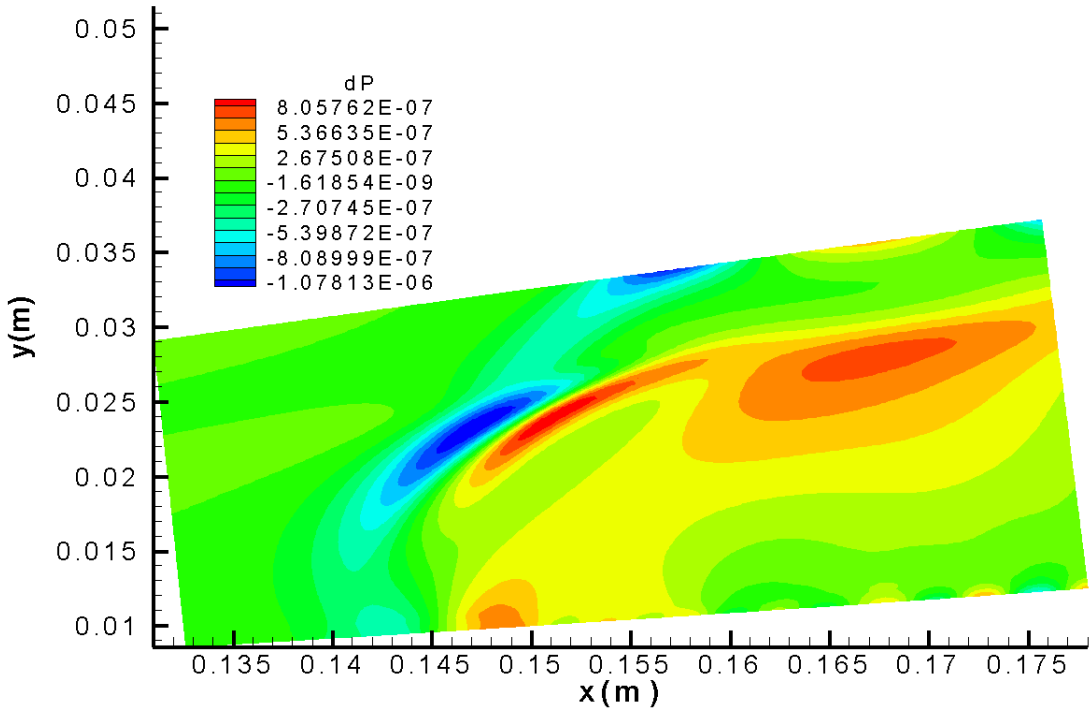

Figure 22. Contour plot of the rear part of hotspot pressure perturbation behind the shock in zone 12

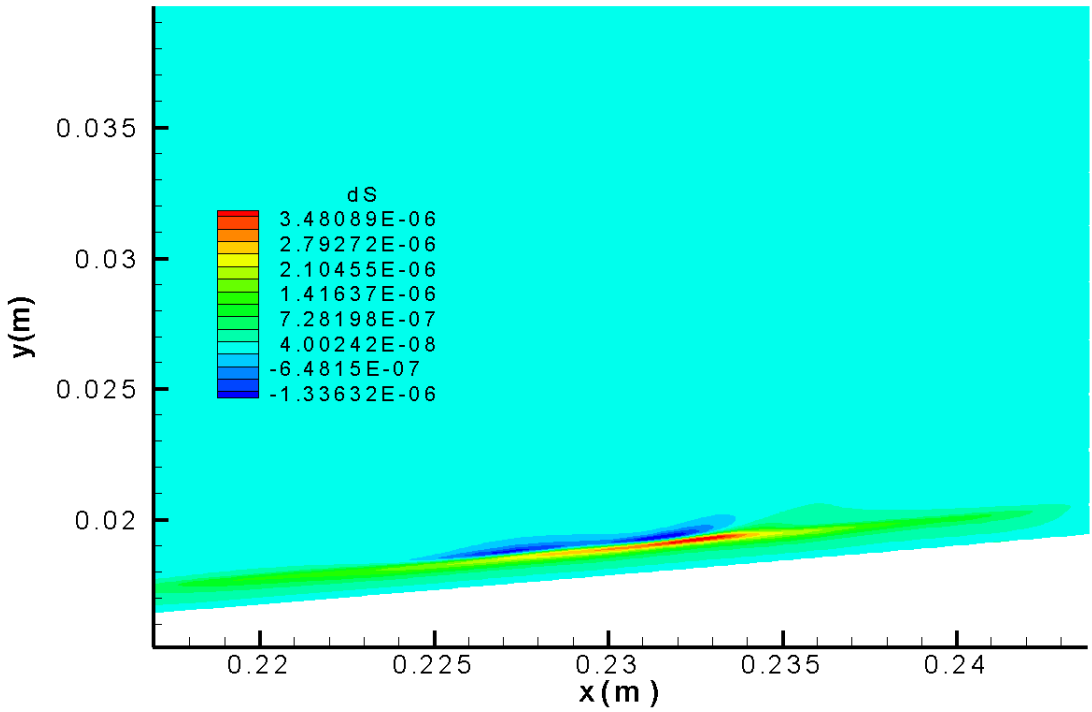

Figure 23. Contour plot of the main body of hotspot entropy perturbation behind the shock in zone 14

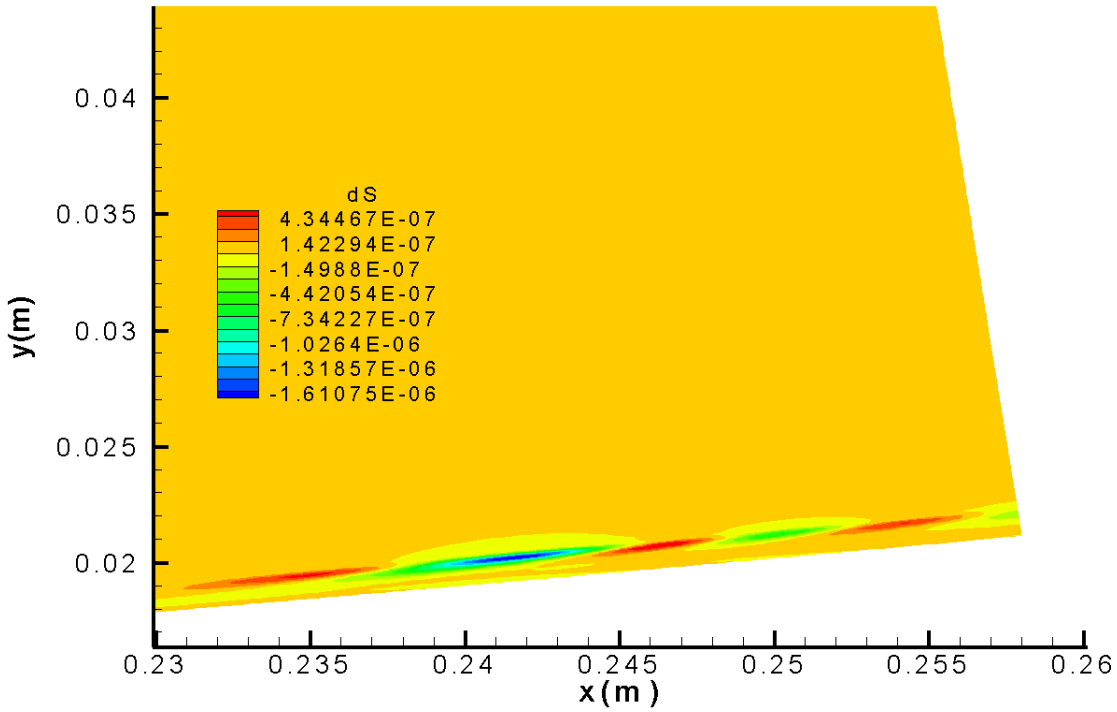

Figure 24. Contour plot of the first tail of hotspot entropy perturbation behind the shock in zone 14

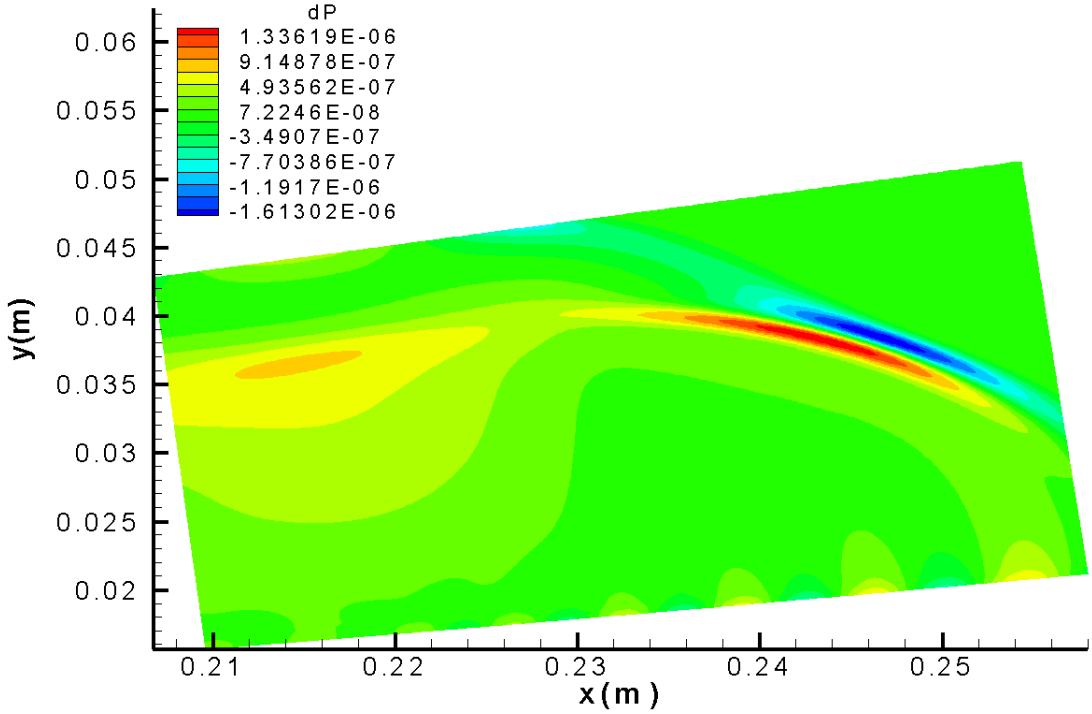

Figure 25. Contour plot of the front part of hotspot pressure perturbation behind the shock in zone 14

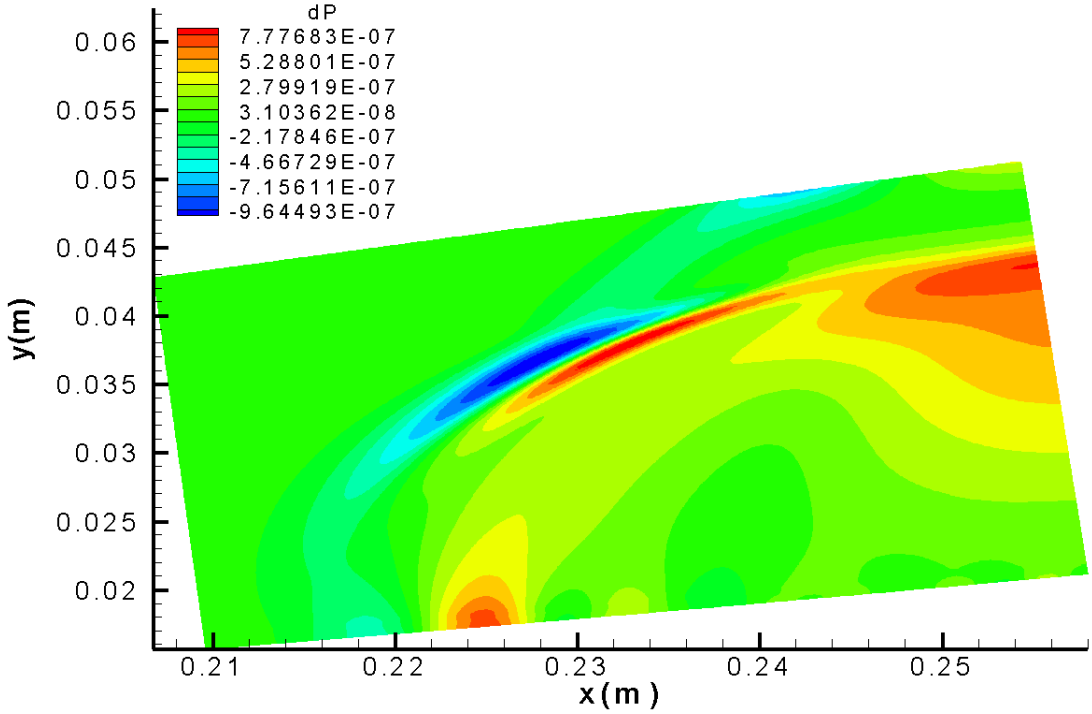

Figure 26. Contour plot of the rear part of hotspot pressure perturbation behind the shock in zone 14

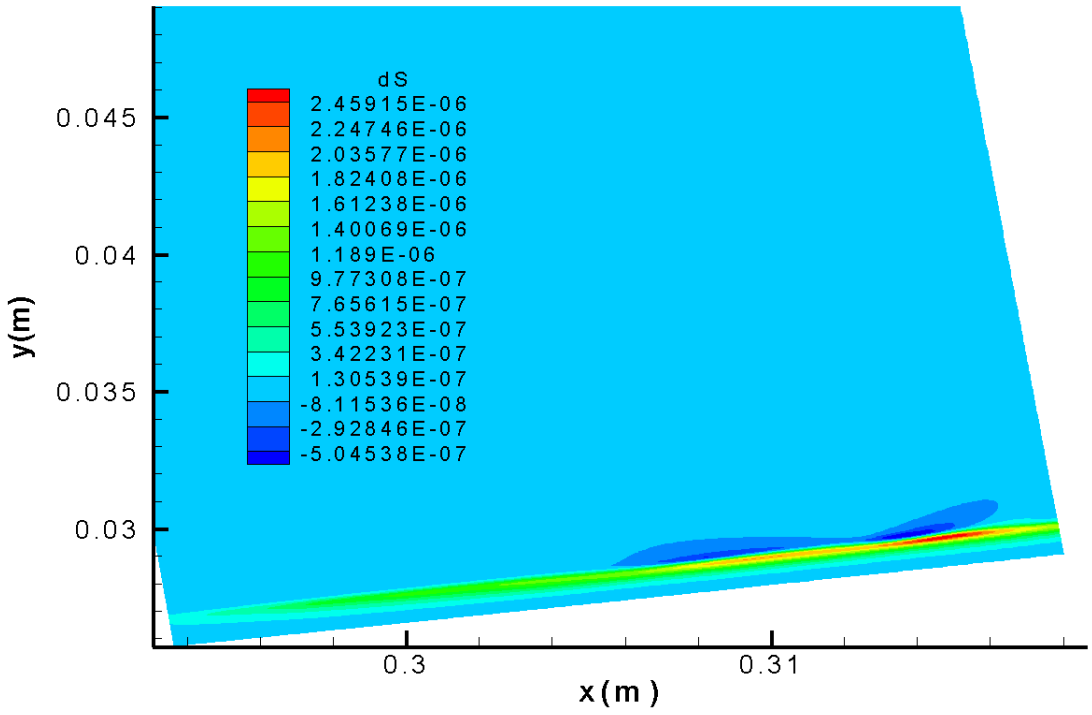

Figure 27. Contour plot of the main body of hotspot entropy perturbation behind the shock in zone 17

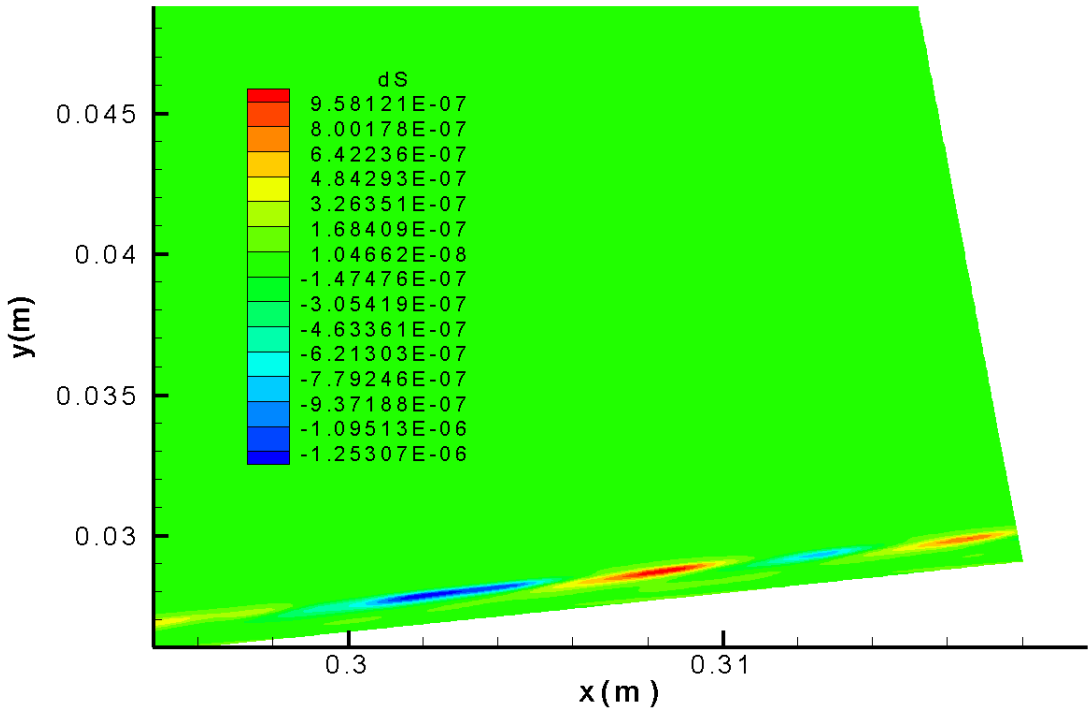

Figure 28. Contour plot of the first tail of hotspot entropy perturbation behind the shock in zone 17

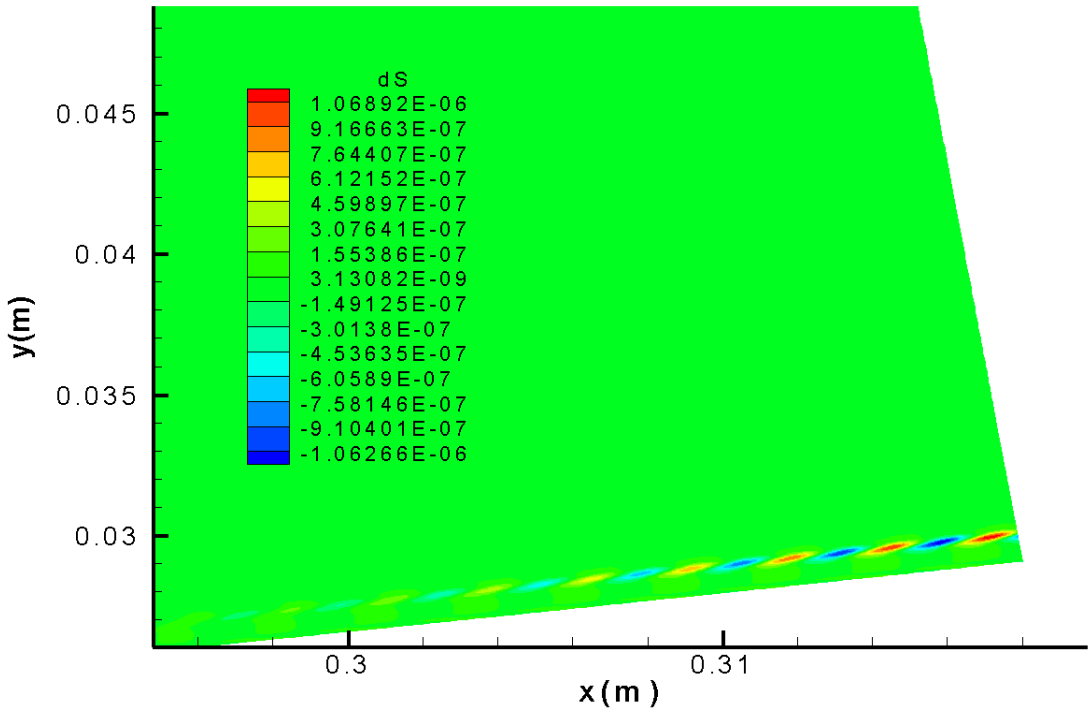

Figure 29. Contour plot of hotspot entropy perturbation second tail in zone 17

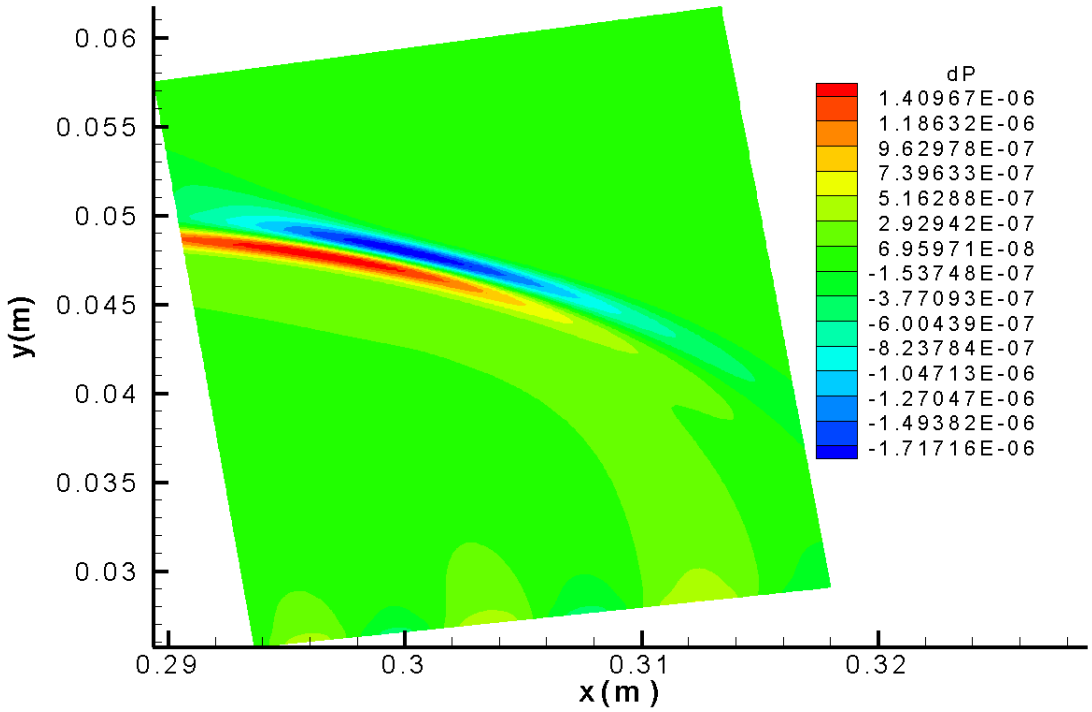

Figure 30. Contour plot of the front part of hotspot pressure perturbation behind the shock in zone 17

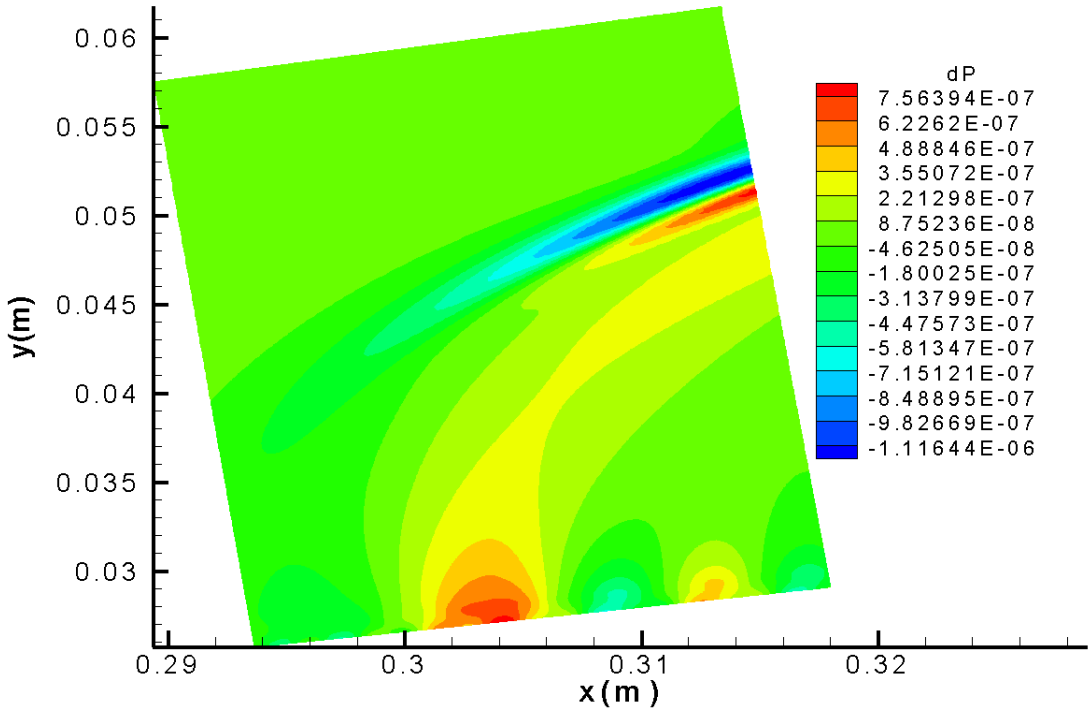

Figure 31. Contour plot of the rear part of hotspot pressure perturbation behind the shock in zone 17

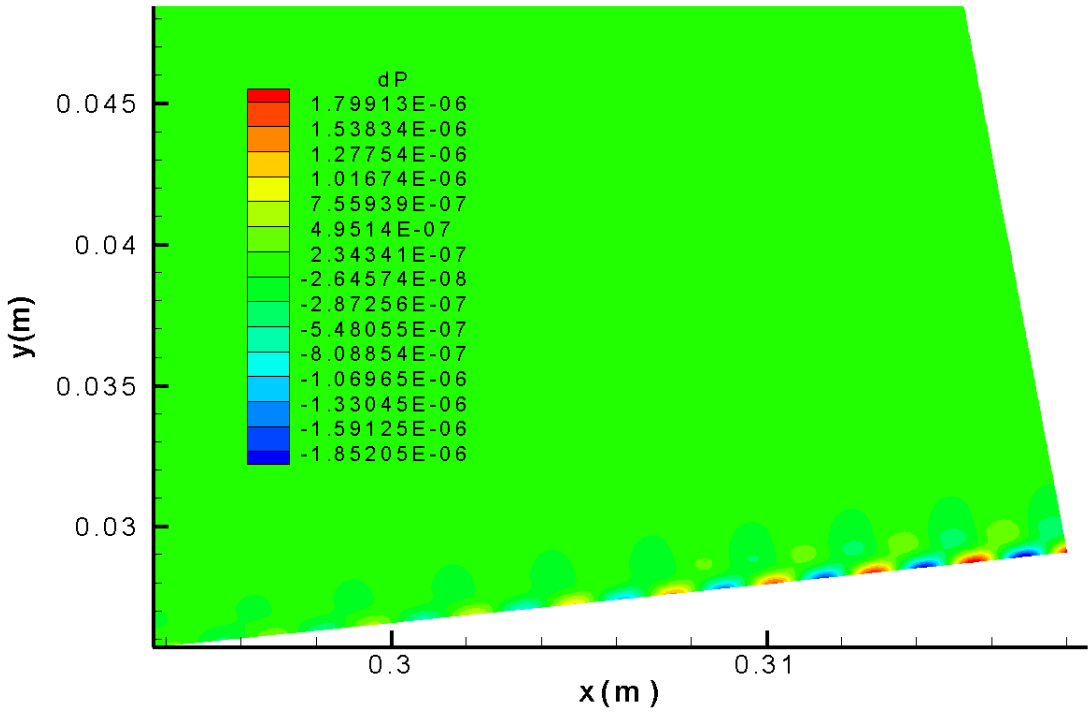

Figure 32. Contour plot of hotspot pressure perturbation tail in zone 17

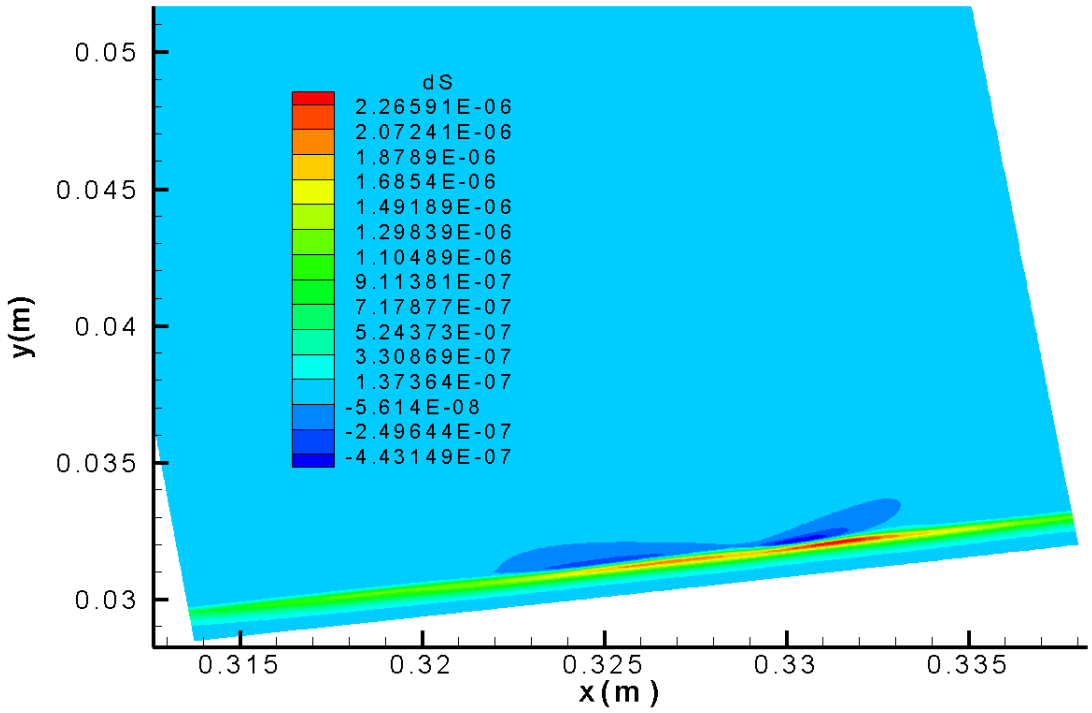

Figure 33. Contour plot of the main body of hotspot entropy perturbation behind the shock in zone 18

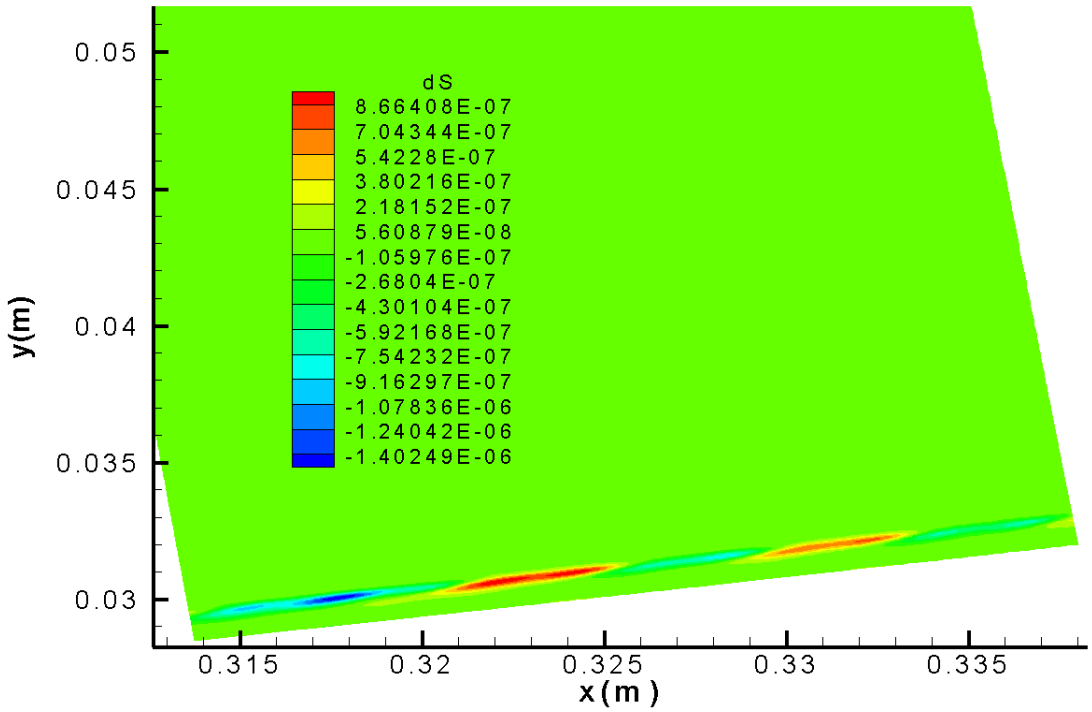

Figure 34. Contour plot of the first tail of hotspot entropy perturbation behind the shock in zone 18

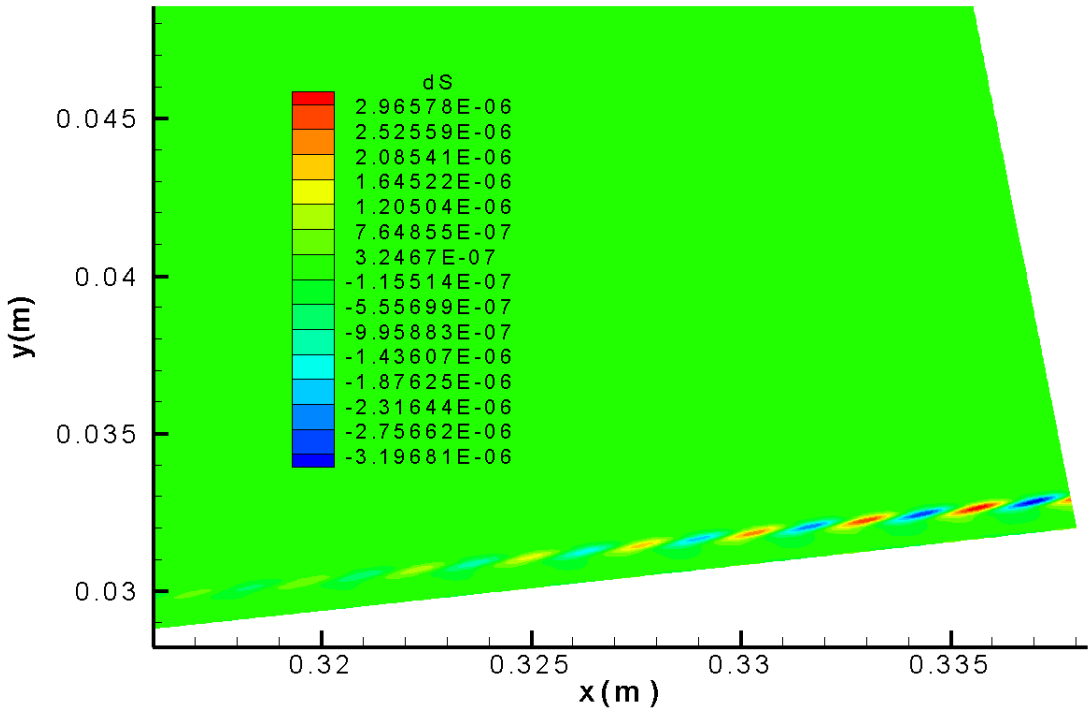

Figure 35. Contour plot of hotspot entropy perturbation second tail in zone 18

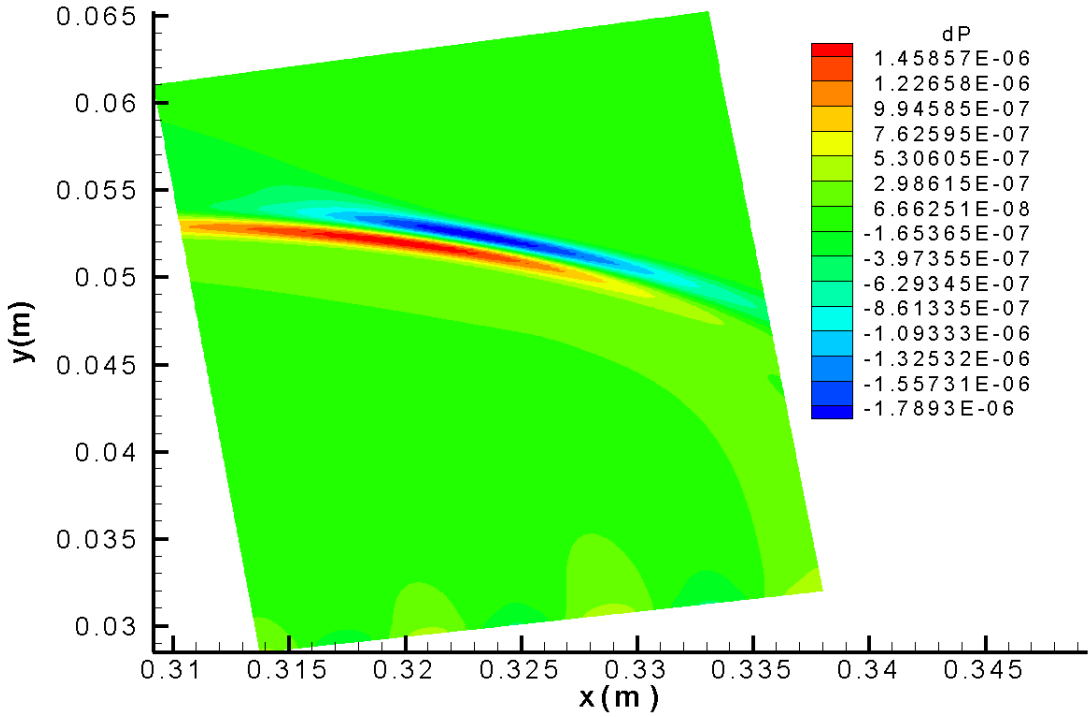

Figure 36. Contour plot of the front part of hotspot pressure perturbation behind the shock in zone 18

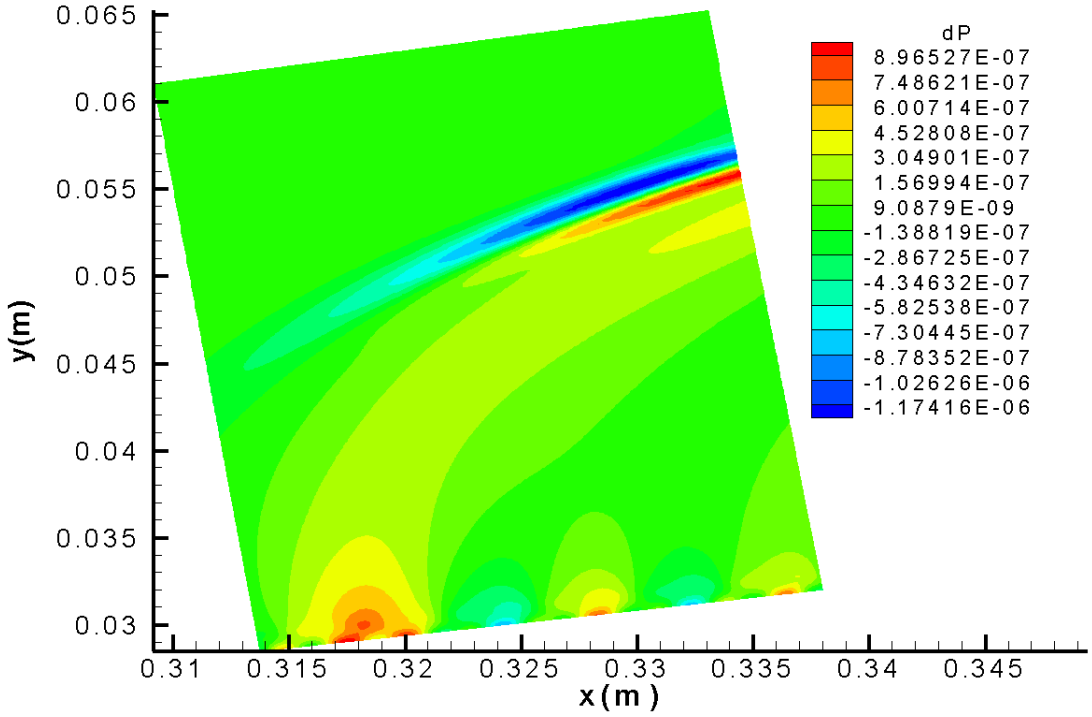

Figure 37. Contour plot of the rear part of hotspot pressure perturbation behind the shock in zone 18

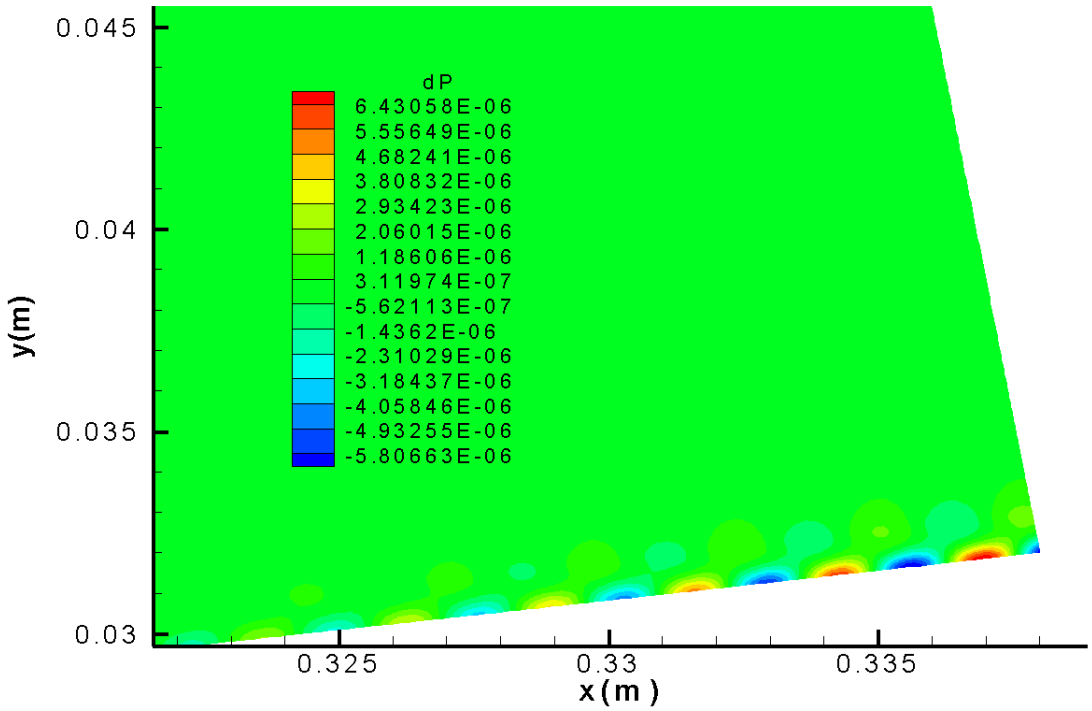

Figure 38. Contour plot of hotspot pressure perturbation tail in zone 18

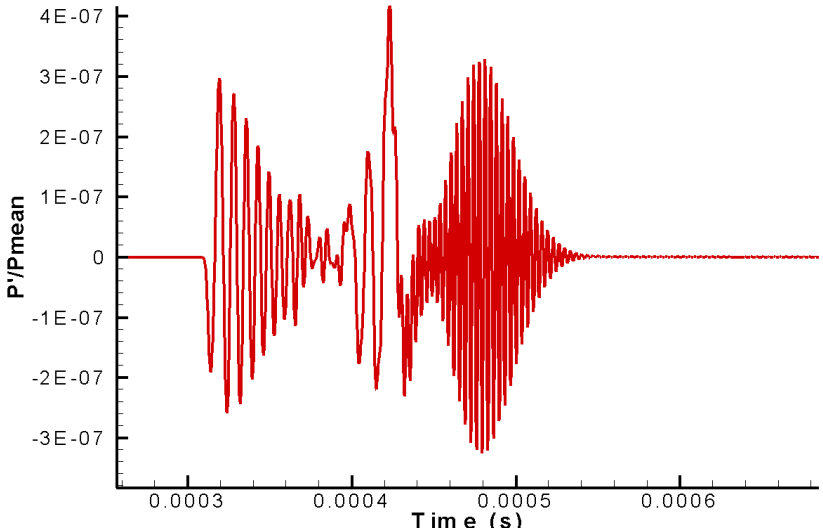

Figure 39. Time-history of wall-pressure perturbation relative to the local mean flow pressure at x=0.313m

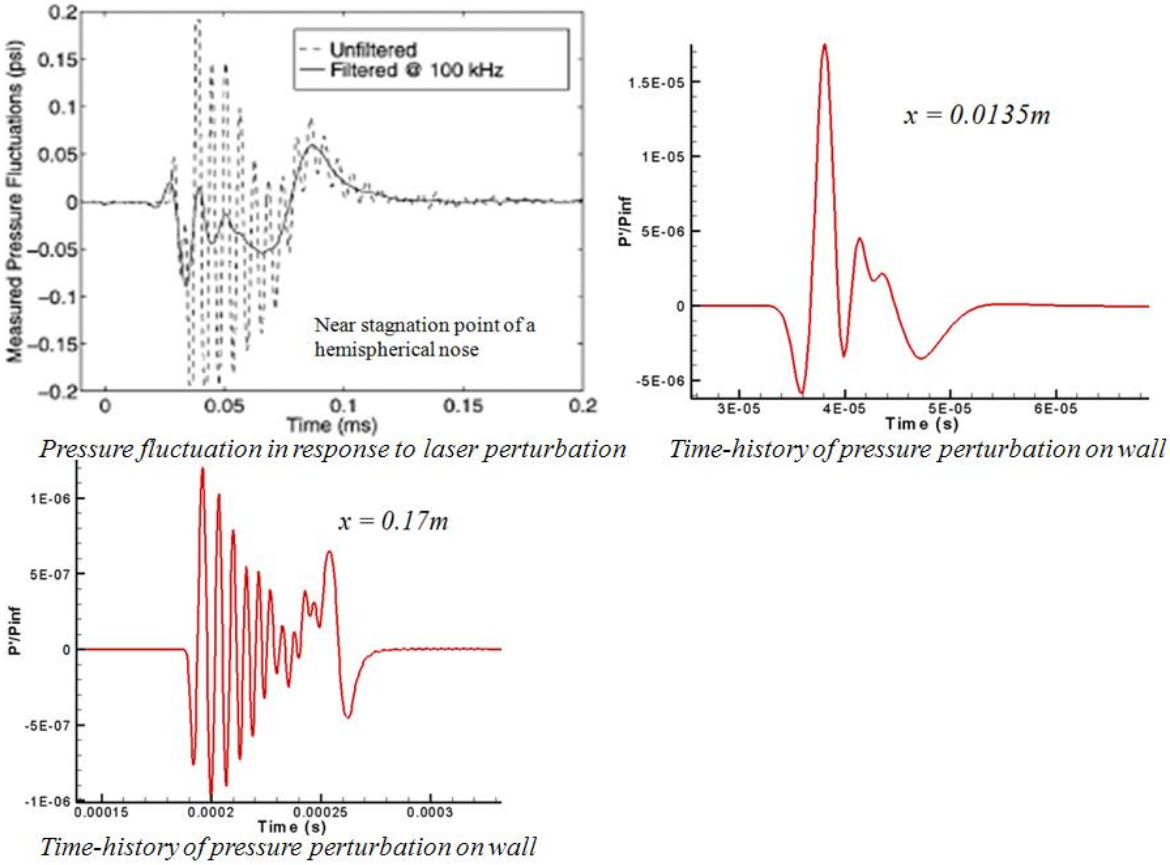

Figure 40. Comparisons of the wall pressure perturbation time-history profile between DNS and experiment [22, 28]

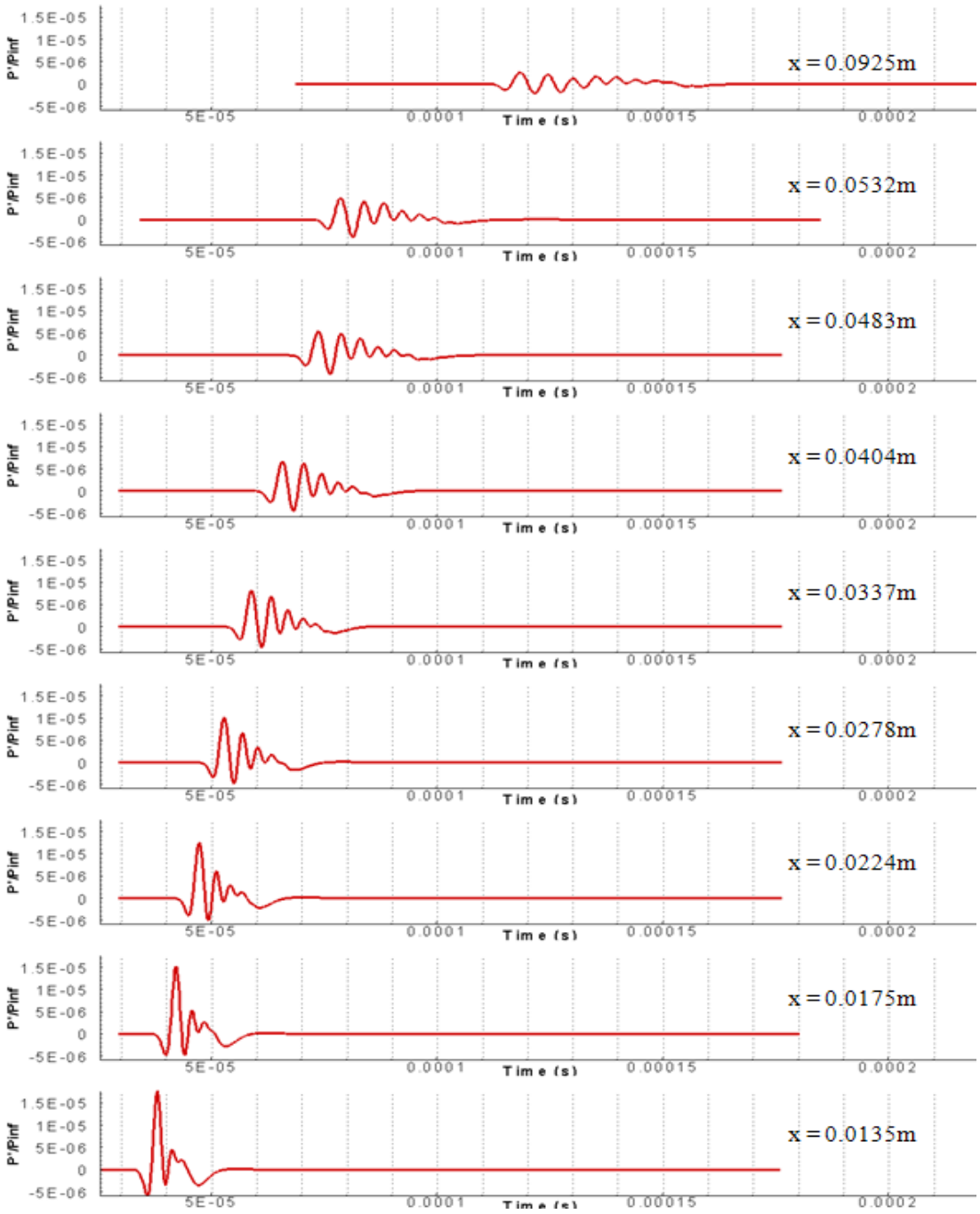

Figure 41. Time-history traces of pressure wall-perturbation at various streamwise locations at upstream part of the cone

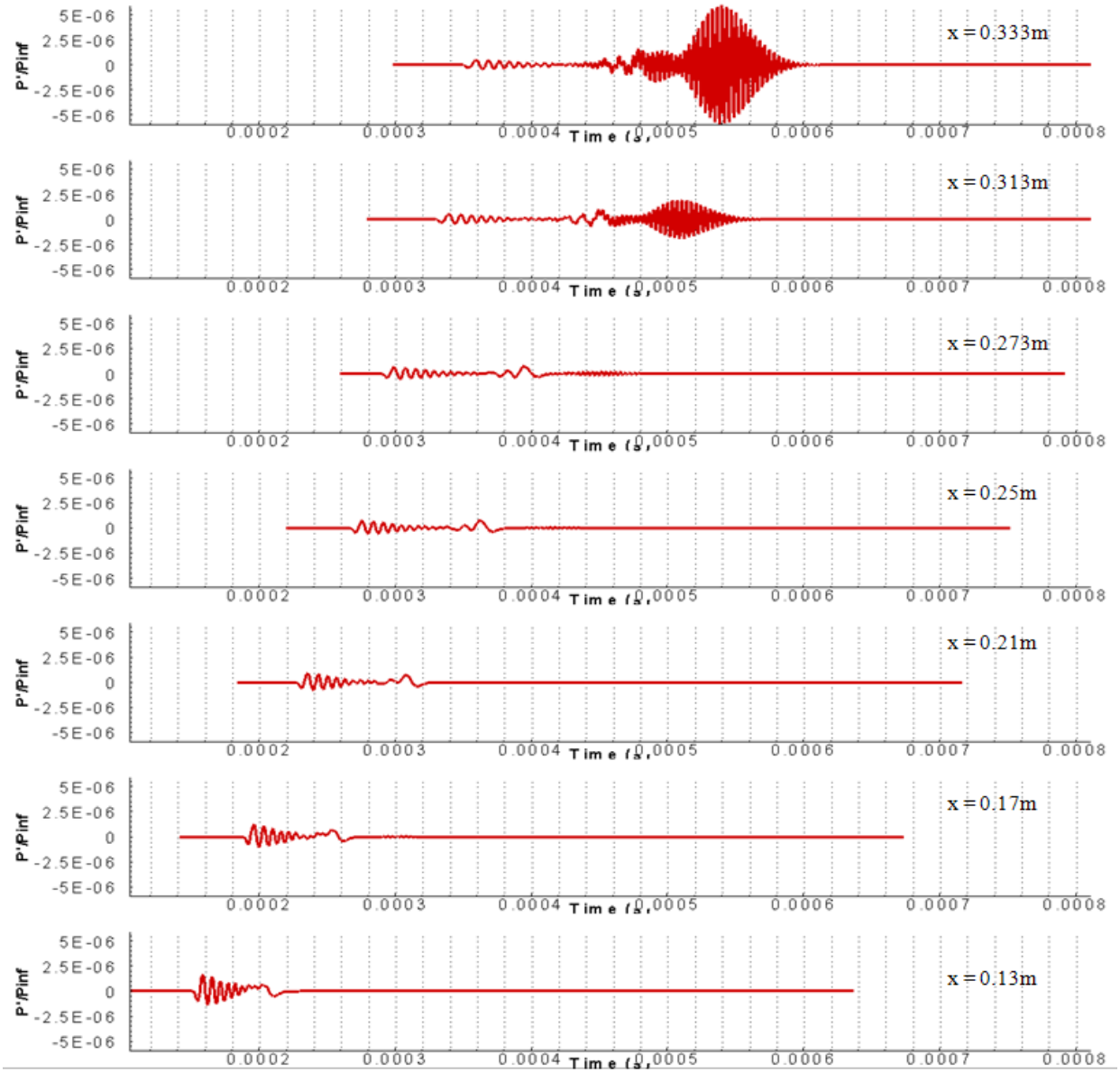

Figure 42. Time-history traces of pressure wall-perturbation at various streamwise locations at downstream part of the cone

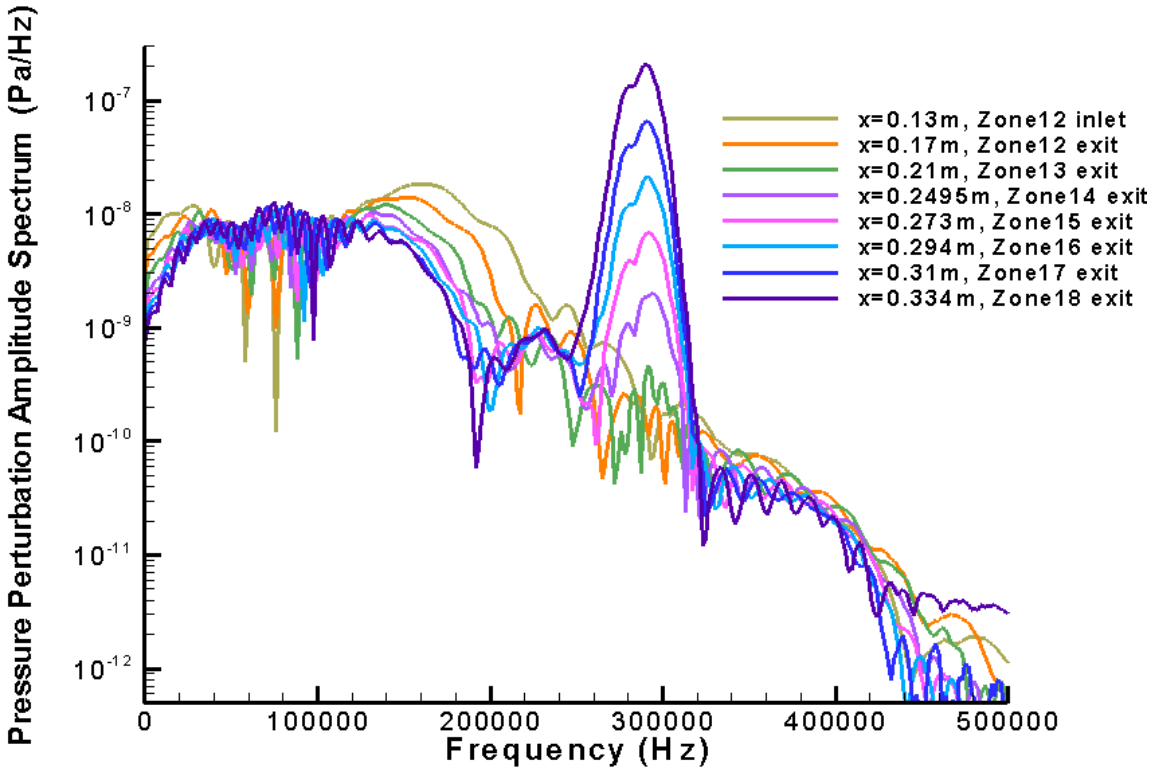

Figure 43. Frequency spectrum of wall pressure perturbation

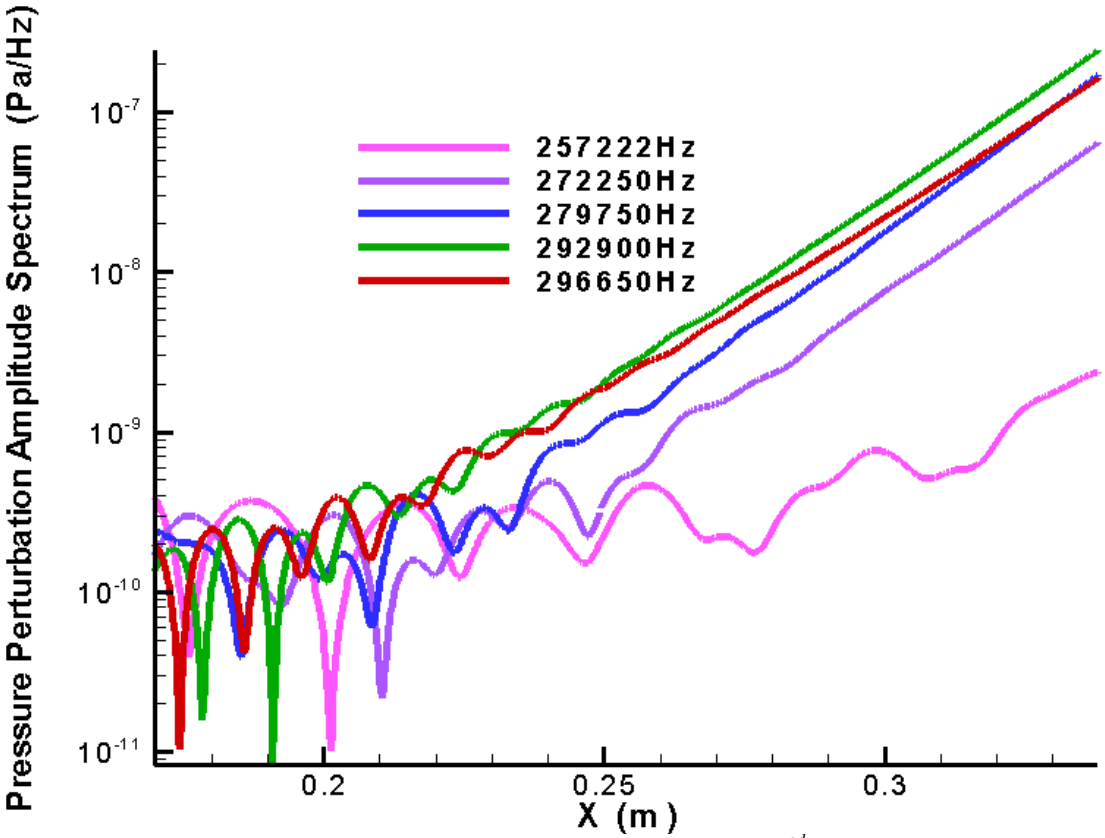

Figure 44. The spatial development of wall pressure perturbation with 2nd mode sampling frequencies in spectral domain

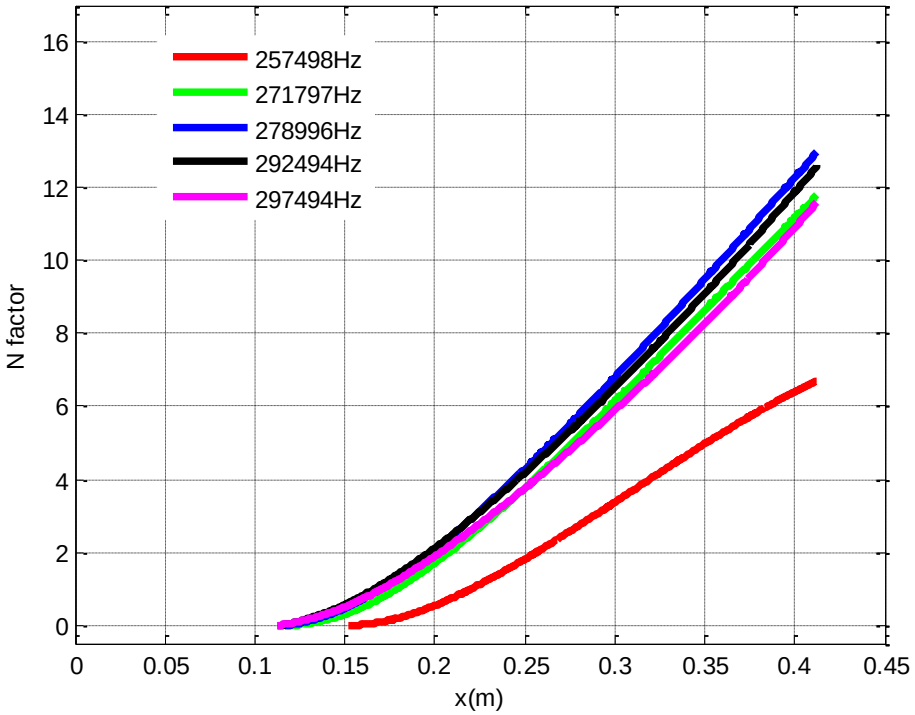

Figure 45. LST N-factor plot [13]

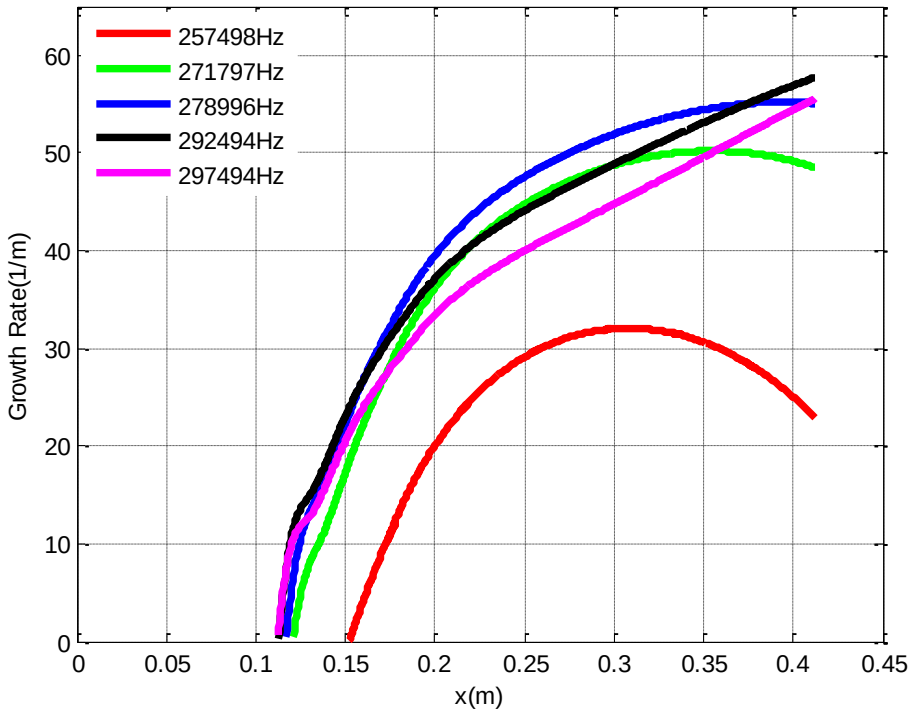

Figure 46. LST Growth rate plot [13]

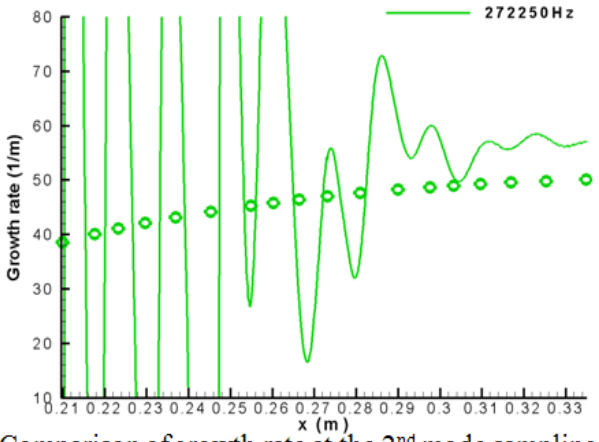

Comparison of growth rate at the 2nd mode sampling frequencies 272250Hz to LST.

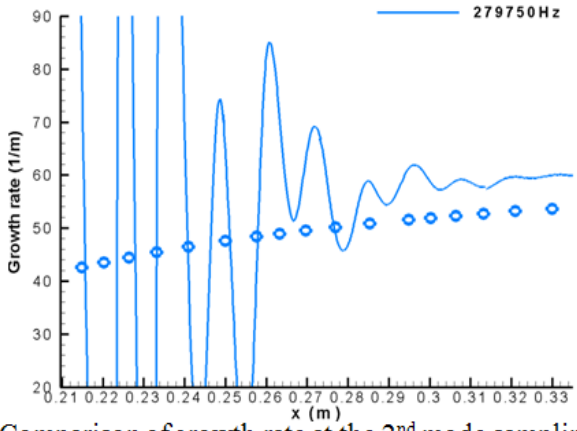

Comparison of growth rate at the 2nd mode sampling frequencies 279750Hz to LST.

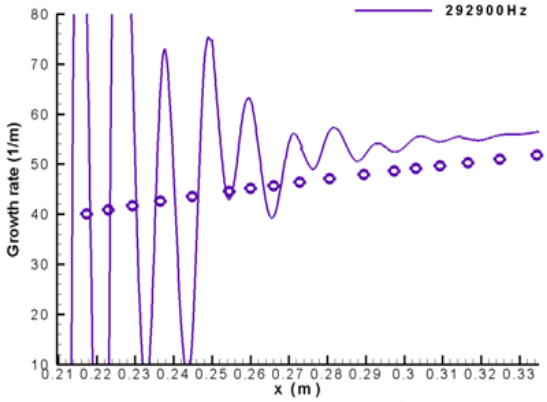

Comparison of growth rate at the 2nd mode sampling frequencies 292900Hz to LST.

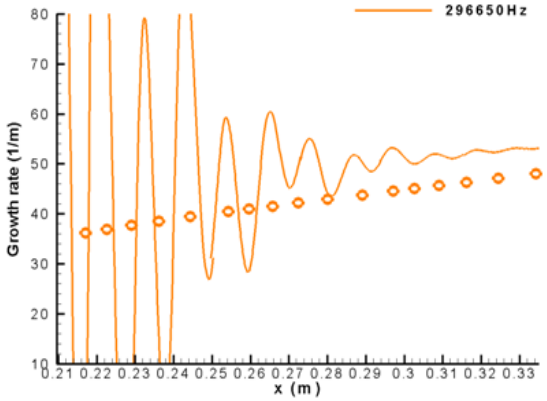

Comparison of growth rate at the 2nd mode sampling frequencies 296650Hz to LST.

Note: Symbols are LST results, lines are DNS results.

Figure 47. Comparisons of growth rate between DNS and LST with various sampling frequencies

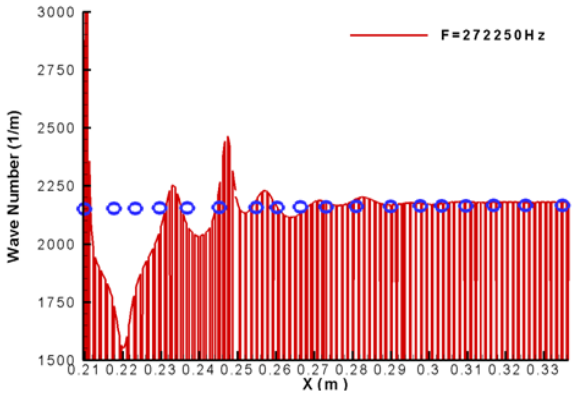

Comparison of DNS wave number spatial development with LST at F=272250Hz.

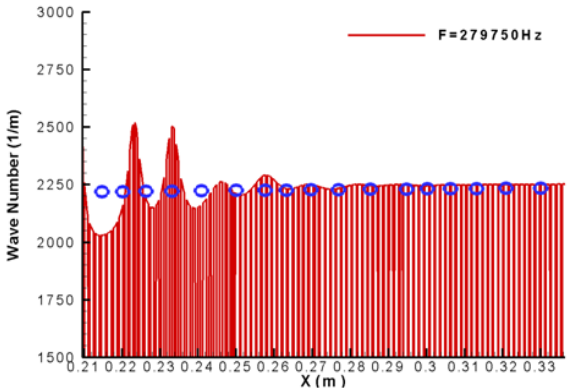

Comparison of DNS wave number spatial development with LST at F=279750Hz.

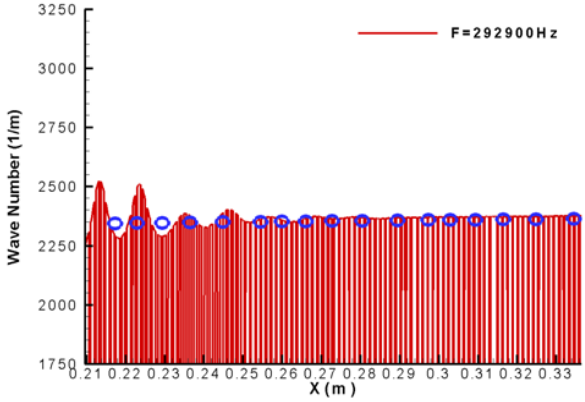

Comparison of DNS wave number spatial development with LST at F=292900Hz.

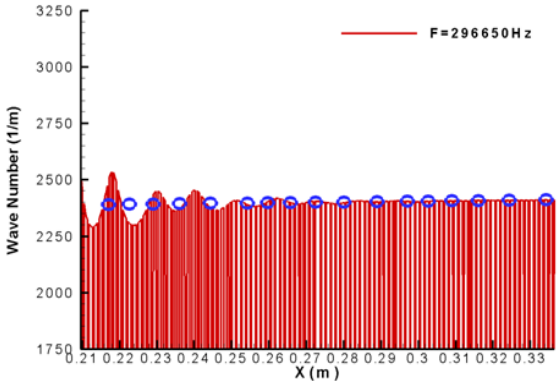

Comparison of DNS wave number spatial development with LST at F=296650Hz.

Note: Symbols are LST results, lines are DNS results.

Figure 48. Comparisons of wave number between DNS and LST with various sampling frequencies

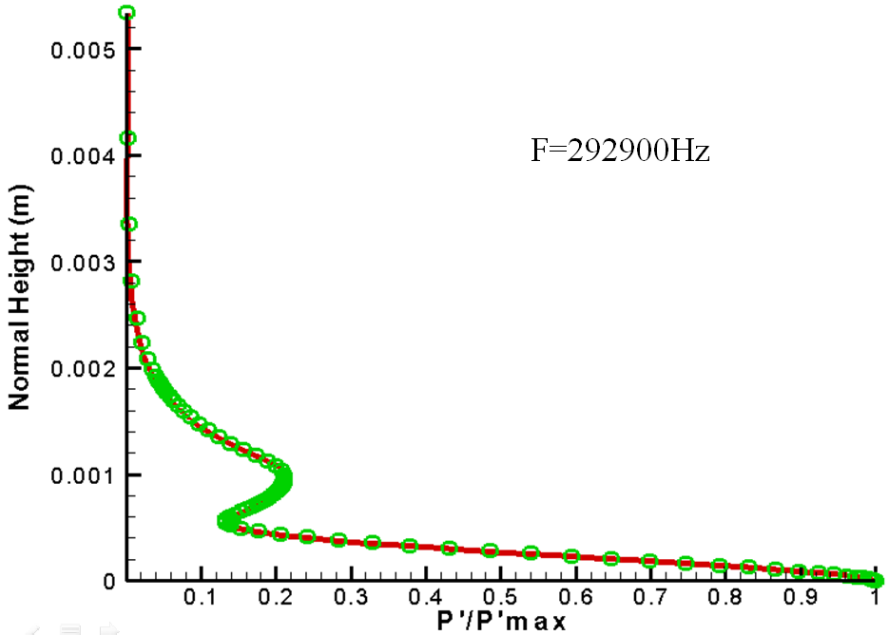

Figure 49. Comparisons of wall-normal mode shape in boundary layer between DNS and LST at x = 0.31115m

Acknowledgments

This work was sponsored by the AFOSR/NASA National Center for Hypersonic Research in Laminar-Turbulent Transition and by the Air Force Office of Scientific Research, USAF, under Grant No. FA9550-07-1-0414, monitored by Dr. John Schmisseur. The views and conclusions contained herein are those of the authors and should not be interpreted as necessarily representing the official policies or endorsements either expressed or implied, of the Air Force Office of Scientific Research or the U.S. Government.

Both authors of this paper specially thank to Professor Steve Schneider at Purdue University and his group for providing the data and information of their compression cone and other wind-tunnel experiments, which make the authors' work more comparable to the real-world experiments.

References

[1] Dunn, J.W., "Numerical Simulation of Bow-Shock/Disturbance Interactions in Mach-4 Flows Past a Hemisphere" AIAA Paper, 98-0007, January 1998.

[2] Reshotko E., "Hypersonic Stability and Transition", Hypersonic Flows for Reentry Problems, Berlin: Springer, 1991.

[3] Salyer, T.R., "Laser Differential Interferometry for Supersonic Blunt Body Receptivity Experiments", PhD Thesis, Purdue University, May 2002.

[4] Salyer, T.R., Collicott, S.H., Schneider, S.P., "Characterizing Laser-Generated Hot Spots for Receptivity Studies", AIAA Journal, Vol.44, No.12, December 2006.

[5] Schneider, S.P., Wheaton, B.M., Julinao, T.J., Berridge, D.C., Chou, A., Gilbert P.L., Casper. K.M., Steen, L.E., "Instability and Transition Measurements in the Mach-6 Quiet Tunnel", AIAA Paper, 2009-3559, June 2009.

[6] Zhong, X. "High-Order Finite-Difference Schemes for Numerical Simulation of Hypersonic Boundary-Layer Transition", Journal of Computational Physics 144,662-709, April 1998.

[7] Zhong, X., "Receptivity of Mach 6 Flow over a Flared Cone to Freestream Disturbance", AIAA Paper, 2004-253, January 2004.

[8] Zhong, X., Lee, T.K., "Nonequilibrium Real-Gas Effects on Disturbance/Bow Shock Interaction in Hypersonic Flow Past a Cylinder", AIAA, 1996.

[9] Schmisseur, J.D., Collicott, S.H., Schneider, S.P., "Laser-Generated Localized Freestream Perturbations in Supersonic and Hypersonic Flows", AIAA Journal, vol. 38, No.4, April 2000.

[10] McKenzie, J. F., Westphal, K. O., "Interaction of Linear Waves with Oblique Shock Waves", The Physics of Fluids, Vol. 11, No. 11, November 1968.

[11] Kovasznay, L. S. G., "Turbulence in Supersonic Flow", Journal of the Aeronautical Sciences, Vol. 20, No. 10, pp. 657-682, October 1953.

[12] Malik, M. R., "Numerical Method for Hypersonic Boundary Layer Stability", Journal of Computational Physics, 86, 376-413, 1990.

[13] Huang, Y., Zhong, X., "Numerical Study of Laser-Spot Effects on Boundary-Layer Receptivity for Blunt Compression-Cones in Mach-6 Freestream", AIAA paper, 2010-4447, June 2010.

[14] Ward, C.A.C., Wheaton, B.M., Chou, A., Gilbert, P.L., Steen, L.E., Schneider, S.P., "Boundary-Layer Transition Measurements in a Mach-6 Quiet Tunnel", AIAA paper, 2010-4721, June 2010.

[15] Chou, A., "Characterization of Laser-Generated Perturbations and Instability Measurements on a Flared Cone", MS Thesis, Purdue University, December 2010.

[16] Ma, Y., Zhong, X., "Receptivity of a Supersonic Boundary Layer over a Flat Plate. Part 3. Effects of Different Types of Free-stream Disturbances", Journal of Fluid Mechanics, vol. 532, pp. 63-109. December 2004.

[17] Pruett, C.D., Chang, C.L., "Direct Numerical Simulation of Hypersonic Boundary-Layer Flow on a Flared Cone", Theoretical and Computational Fluid Dynamics (1998) 11:49-67, Springer-Verlag 1998.

[18] Balakumar, P., Kegerise, M.A., "Receptivity of Hypersonic Boundary Layers over Straight and Flared Cones", AIAA paper, 2010-1065, January 2010.

[19] Mack, L.M., "Boundary Layer Linear Stability Theory", AGARD report, No. 709, pp.3-1 to 3-81, 1984.

[20] Press et al, "Numerical Recipes The Art of Scientific Computing", Cambridge University Press 1986.

[21] Sivasubramanian, J., Fasel, H.F. "Numerical Investigation of Boundary-layer Transition Initiated by a Wave Packet for a Cone at Mach 6", AIAA paper, 2010-900, January 2010.

[22] Randall, L. A., "Receptivity Experiments on a Hemispherical Nose at Mach 4", M.S. Thesis, School of Aeronautics and Astronautics, Purdue Univ., W. Lafayette, IN, 1996.

[23] Stetson, K.F., Thompson, E.R., Donaldson, J.C., Siler, L.G., "Laminar Boundary Layer Stability Experiments on a Cone at Mach 8, Part 2: Blunt Cone", AIAA paper, 84-0006, January 1984.

[24] Sivasubramanian, J., Mayer, C.S.J., Laible, A.C., Fasel, H.F., "Numerical Investigation of Wavepackets in a Hypersonic Cone Boundary Layer at Mach 6", AIAA paper, 2009-3560, June 2009.

[25] Sivasubramanian, J., Fasel, H. F., "Direct Numerical Simulation of a Turbulent Spot in a Cone Boundary-Layer at Mach 6", AIAA paper, 2010-4599, June 2010.

[26] Sivasubramanian, J., Fasel, H. F., "Transition Initiated by a Localized Disturbance in a Hypersonic Flat-Plate Boundary Layer", AIAA paper, 2011-374, January 2011.

[27] Salyer, T.R., Collicott, S.H., Schneider, S.P., "Feedback Stabilized Laser Differential Interferometry for Supersonic Blunt Body Receptivity Experiments", AIAA paper, 2000-0416, January 2000.

[28] Ladoon, D.W., Schneider, S.P., Schmisseur, J.D., "Physics of Resonance in a Supersonic Forward-Facing-Cavity", Journal of Spacecraft and Rockets, vol. 35, No. 5, September-October 1998.

[29] Chou, A., Wheaton, B.M., Ward, C.A.C., Gilbert, P.L., Steen, L.E., Schneider, S.P., "Instability and Transition Research in a Mach-6 Quiet Tunnel", AIAA paper, 2011-283, January 2011.

[30] Schneider, S.P., Collicott, S.H., "Laminar-Turbulent Transition in High-Speed Compressible Boundary Layers: Continuation of Elliptic-Cone Experiments", Final Report, School of Aeronautical and Astronautical Engineering, Purdue Univ. W. Lafayette, IN, January 2000.

[31] Casper, K.M., Beresh, S.J., Schneider, S.P., "Pressure Fluctuations beneath Turbulent Spots and Instability Wave Packets in a Hypersonic Boundary Layer", AIAA paper, 2011-372, January 2011.

[32] Schmisseur, J.D., "Receptivity of the Boundary Layer on a Mach 4 Elliptic Cone to Laser-Generated Localized Free Stream Perturbations", PhD Thesis, Purdue Univ., W. Lafayette, IN, December 1997.

[33] Heitmann, D., Kahler, C.J., Radespiel, R., "Installation of a System for Laser-Generated Perturbations in Hypersonic Flow", 14th International Symposium on Application of Laser Techniques to Fluid Mechanics, July 2008.

[34] Heitmann, D., Kahler, C.J., Radespiel, R., "Investigation of Laser Generated Perturbations for Boundary Layer Stability Experiments", Numerical & Experimental Fluid Mechanics VII, NNFM 1112, pp. 297-305, Springer-Verlag Berlin Heidelberg 2010.

[35] Heitmann, D., Kahler, C.J., Radespiel, R., Rodiger, T., Knauss, H., Wagner, S., "Non-Intrusive Generation of Instability Waves in a Planar Hypersonic Boundary Layer", Exp Fluids, 50:457-464, Springer-Verlag 2010.

[36] Heitmann, D., Radespiel, R., Kahler, C.J., "Investigation of the Response of a Hypersonic 2D Boundary Layer to Controlled Acoustic Disturbances", AIAA paper, 2010-536, January 2010.

[37] Heitmann, D., Kahler, C.J., Radespiel, R., "Investigation of Laser-Generated Flow Perturbations in Hypersonic Flow over a Flat Plate", AIAA paper, 2008-3737, June 2008.